# Design and Fabrication of Polyvinylidene Fluoride for Triboelectric Nanogenerators

**Hossein Abdoli**

A THESIS SUBMITTED TO

THE FACULTY OF GRADUATE STUDIES

IN PARTIAL FULFILLMENT OF THE REQUIREMENTS

FOR THE DEGREE OF

MASTER OF APPLIED SCIENCE

Graduate Program in

MECHANICAL ENGINEERING

York University

Toronto, Ontario

August 2019

# Abstract

Recently triboelectric nanogenerators (TENGs) have attracted huge interest because of their flexibility to harvest wasted mechanical energy. However, triboelectrification is a well-known phenomenon for centuries, the underlying physics behind it is still under debate, so a comprehensive study on triboelectrification is needed. Herein, effects of polyvinylidene fluoride (PVDF) friction layer's thickness, contact area and porosity on TENG's performance were investigated. Results showed that increasing surface area or decreasing thickness of friction layer positively affected the performance of TENG. This is mainly attributed to improvement of PVDF charge density. Then, for further enhancement of TENG's performance, electroactive phase content of PVDF enhanced using different fabrication methods such as supercritical $CO_2$ processing, non-isothermal crystallization, electro-poling and electrospinning. The results confirmed increasing in PVDF electroactive phase content positively affected triboelectric properties. Consequently, by fabrication of chitin-PVDF electrospun film the average of voltage and current density increased to 72.8 V and 6.47 $mA/m^2$, respectively.

# Acknowledgment

There are number of people who did everything for me to support my master studies at Mechanical Engineering Department of York University. At very first, I would love to say thanks to my supervisor, Professor Siu Ning Sunny Leung, indeed this research was impossible without his guidance. I am so grateful to him since he made my student life much more easier by all of his emotional support, encouragement and providing a light path for my research in Multifunctional Materials, Micro-and-Nanostructuring Laboratory.

I need to express my gratitude to my master thesis committee member, Professor Garrett Melenka from Mechanical Engineering Department, for all his support within my course of master studies, especially for his favor to help with μ-CT analysis. I would like to thank Professor Simone Pisana from Electrical Engineering Department, for his feedback on my thesis and oral examination.

I am also grateful for the funding support for this research from Natural Sciences and Engineering Research Council (NSERC) of Canada and York University.

I would like to thank my colleagues and friends in Mechanical Engineering Department because of all their contribution, friendship and patronage within my research.

At the end, I want to say thank to my beloved family. My parents and brothers, Hamed and Erfan took my back every day from miles away and there is no word to describe how supportive they were for me in the last two years. I also owe a big thanks to my BFF, Sam, he was the one who always encouraged me and helped me to make the right decisions and go through my most difficult times successfully.

# Table of Contents

# List of Tables

# List of Figures

# List of Abbreviations

| | |
|---|---|
| A | Absorbance band |
| AC | Alternating current |
| C | Capacitance |
| $CO_2$ | Carbon dioxide |
| d | Thickness |
| DC | Direct current |
| DSC | Differential scanning calorimetry |
| E | Electrical field |
| Eq. | Equation |
| F | Fraction |
| FTIR | Fourier transform infrared spectroscopy |
| I | Current |
| M | Mass |
| NA | Not applicable |
| NaCl | Sodium chloride |
| OC | Open circuit |
| OH | Hydroxyl group |
| PDMS | Polydimethylsiloxane |
| PVDF | Polyvinylidene fluoride |
| Q | Electrical charge |
| $Q_{TE}$ | Triboelectrification charge |
| S | Contact area |
| SC | Short circuit |
| $ScCO_2$ | Supercritical $CO_2$ |
| SEM | Scanning electron microscopy |
| T | Temperature |
| TENG | Triboelectric nanogenerator |

| | |
|---|---|
| V | Voltage |
| VER | Volume expansion ratio |
| Vg | Geometric volume |
| Vt | Total volume |
| x(t) | Air gap (where t represents time) |
| $X_c$ | Degree of crystallinity |
| $\alpha$ | Alpha crystal phase |
| $\beta$ | Beta crystal phase |
| $\gamma$ | Gamma crystal phase |
| $\varepsilon_r$ | Relative permittivity (Dielectric constant) |
| $\varepsilon_0$ | Vacuum permittivity |
| $\sigma$ | Charge density |
| $\rho$ | Density |
| $\Delta H_f$ | Heat of fusion of PVDF sample |
| $\Delta H_{f,c}$ | Heat of fusion of 100% crystalline PVDF (*i.e.*, 104.7 J/gr) |
| $\Delta H_\beta$ | Difference in the height of the absorbance bands from the FTIR Peak at 1275 $cm^{-1}$ to its nearest valley |
| $\Delta H_\gamma$ | Difference in the height of the absorbance bands from the FTIR Peak at 1234 $cm^{-1}$ to its nearest valley |

# Chapter 1 Introduction

## 1.1 Background

Harvesting wasted mechanical energy and converting it to electricity is one potential solution for the recent energy crisis around the world [1]. Although some technologies based on electrostatic, electromagnetism, and piezoelectricity had been introduced to generate electricity out of wasted mechanical energy, triboelectric nanogenerators (TENGs) was only introduced in 2012 for the first time [2-3].

Triboelectric nanogenerator fundamentally works by conjunction of triboelectrification effect and electrostatic induction [4]. As Figure 1.1 shows, based on triboelectric effect when two materials with different triboelectric properties touch each other, electrons will transfer from one surface to the other. Consequently, one of them becomes positively charged and the other becomes negatively charged. While the other side of TENG friction layers is attached to electrodes, the whole system is in equilibrium as long as the charged surfaces are in contact. Once the charged surfaces begin to separate, a potential difference between plates will appear. As a result of electrostatic induction, the potential difference between plates will lead to a flow of electrons in an external circuit between two electrodes in order to compensate for the potential difference and to restore equilibrium. By removing the gap between plates, the potential difference will vanish and the electrons will flow back to their original position again. Periodic contact and separation of charged surface will thereby generate AC current in the external circuit [5]. Although triboelectrification is a well-known phenomenon for many years, the mechanism behind it is still being investigated with debates and the effect of different parameters on electrification is not thoroughly clear [3].

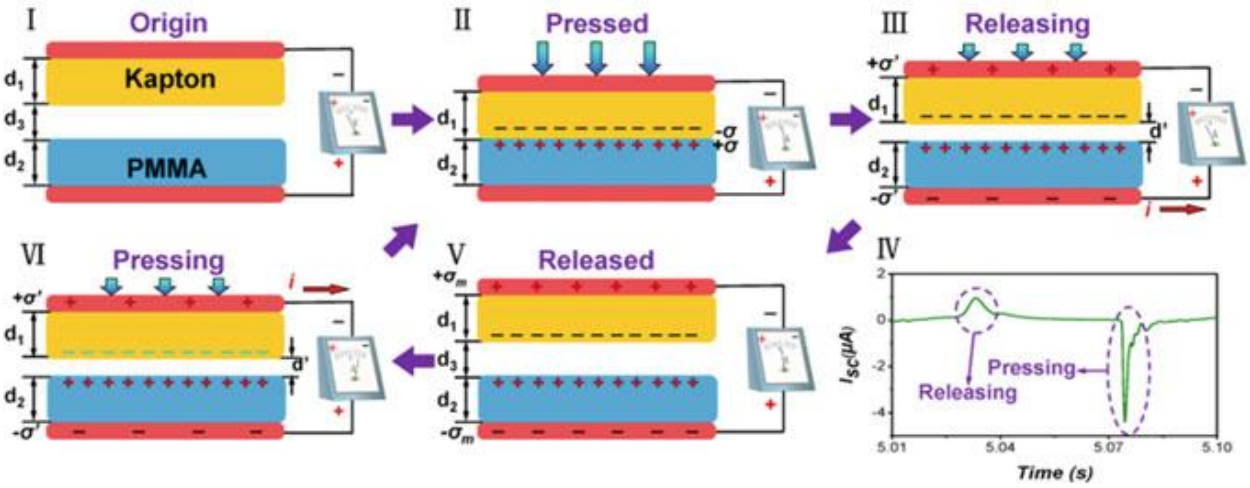


**Figure 1.1 Principle of triboelectric nanogenerator operation [3]. Copyright 2012. Reproduced with permission from American Chemical Society.**

TENG is a powerful technology to harvest various types of mechanical energy such as rain droplets, wind energy, human body motion and *etc*. It also can act as a power source in small self-powered electronic devices [3]. Improvement of TENG's efficiency needs a comprehensive study on the effect of different involved parameters in TENG design.

## 1.2 Polyvinylidene Fluoride (PVDF)

Polyvinylidene fluoride (PVDF) is an inexpensive, non-toxic polymer with pyroelectric, piezoelectric, and triboelectric properties [6]. In addition, PVDF is known for its semi-crystalline structure. Generally, PVDF has five distinct crystal structures such as $\alpha$, $\beta$, $\gamma$, $\delta$ and $\varepsilon$. Among them The presence$\alpha$ trans-gauche-trans-gauche (TGTG′), $\beta$ all-trans planar zigzag (TTT) and $\gamma$ ($T_3GT_3G'$) are extensively investigated [7]. The $\alpha$ is the most common non-polar and stable polymorph in PVDF structure while $\beta$ and $\gamma$ are polar polymorphs. As Figure 1.2 displays, PVDF has a strong dipole moment that is perpendicular to its chains because of the presence of fluorine atoms with much higher electronegativity comparing to carbon and hydrogen atoms. $\beta$ polymorph

possesses the highest dipole moment and most of the researches around PVDF focused on promoting the $\beta$ phase content of PVDF [8].

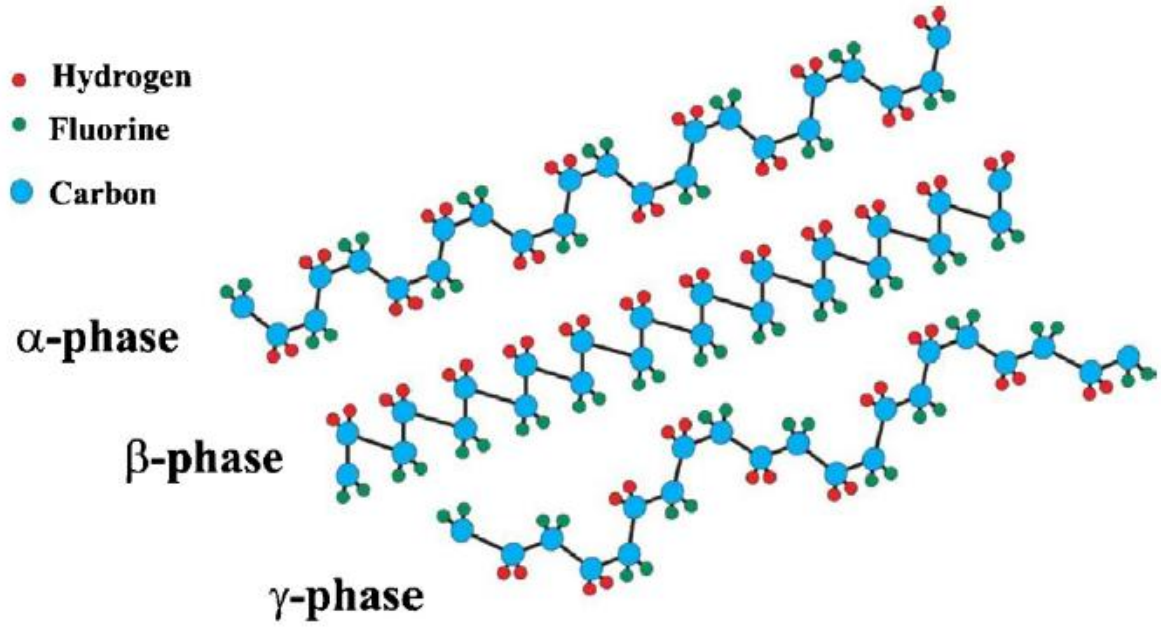


**Figure 1.2 The α, β and γ structure of PVDF [9]. Copyright 2014. Reproduced with permission from Elsevier.**

Special properties of PVDF make it one of the most remarkable polymers to be used as the negative side of friction layer beside other options such as polydimethylsiloxane (PDMS), polyethylene terephthalate (PET), high density polyethylene (HDPE) and polytetrafluoroethylene (PTFE) [3], [10], [11].

## 1.3 Research Motivation

Triboelectric nanogenerator (TENG) is a newly explored technology that can provide enough power for small electronic devices. A comprehensive study of different parameters of TENG is necessary to enhance its efficiency on energy conversion. TENG electrical outputs can be affected

by various parameters such as the surface charge density, chemical composition[12], surface area[13], thickness[14], surface structure[15], applied force[13] and *etc*. Triboelectric's capacity can be modified by changing the geometry of friction layers [16]. Furthermore, fabrication of PVDF foam structure can positively increase the surface charge density and TENG electrical outputs [13]; however, the most important characterization of PVDF is its tunable crystal structure. Researches around PVDF mainly intend to elucidate the piezoelectricity characterization of PVDF [9]. Herein, we enhanced PVDF electroactive phase content by an inexpensive and scalable method and hypothesized that PVDF with higher electroactive content would enhance its piezoelectric and triboelectric properties. Promotion of PVDF electroactive phase content commonly achieved by mechanical stretching of non-polar polymorphs (*i.e.*, $\alpha$) [8], [17], melting and resolidifying under specific conditions [18], addition of nucleating agents [19], ultra-fast cooling [20], applying external electrical field [21] or developing PVDF copolymers [22], which are usually expensive and time-consuming.

## 1.4 Thesis Structure

The first chapter provides the background and motivation of this thesis research. It mainly summarizes TENG history and fundamental as well as PVDF specific characterization as negative side of TENG friction layer. The second chapter is a comprehensive literature review and it covers the major researches about TENG's different modes of operation, effective parameters that influence TENG's performance, fabrication of PVDF with high electroactive phase content, and its capability to be used in TENG. The third chapter extensively discusses the effect of friction layer thickness, contact area and open cell structure of PVDF on TENG performance and the fourth chapter reviews the effects of non-isothermal crystallization and supercritical $CO_2$ processing following by electro-poling on PVDF electroactive phase content on the energy conversion

performance of TENG. Chapter five discusses the use of electrospinning as a potential method to fabricate thin PVDF films and ends with the use of chitin (*i.e.*, a bio-based nanoparticle) as filler to enhance PVDF electroactive phase content and TENG performance. Finally, chapter six briefly concludes the results and contributions of this research and suggests some future direction for this research.

# Chapter 2 Literature Review

This chapter firstly reviews different working modes of TENG, then subsequently summarizes effective parameters that affect TENG performance and different strategies to increase the efficiency of TENG. In addition, common methods to promote electroactive phase content of PVDF are reviewed and the chapter ends with explaining the main objectives of this research.

## 2.1 Triboelectric Nanogenerator Operating Modes

### 2.1.1 Contact and Separation Mode

Most common operating mode for TENG is the contact and separation mode (Figure 1). In contact and separation mode, two materials with different triboelectric properties get in contact. Based on their different tendency to gain or lose electron, they exchange charge on their surfaces. It should be mentioned that the system is in equilibrium as two materials are in contact. A potential difference occurs by separating the surfaces and as a result, electrons flow from one electrode to the other in an external circuit to restore equilibrium. When two surfaces contact again, the potential between them will decrease and electrons will flow back in the reverse direction. Contact and separation of these two charged surfaces, periodically, would result in the generation of AC current in the external circuit (Figure 1.1) [3], [14], [23].

### 2.1.2 Lateral Sliding Mode

The configuration of the lateral sliding mode is shown in Figure 2.1. Similar to the contact and separation mode, two surfaces will share charge on their surfaces (Figure 2.1 (a)). When one plate slides outward, a potential difference appears between charged plates. As a result, free electrons from one electrode will flow to the other electrode to reach an equilibrium state and compensate for the potential difference (Figure 2.1 (b) and (c)). While the plates slide back to their original

positions, the potential difference between plates gradually vanishes and electrons flow back (Figure 2.1 (d)). Consequently, by repeadedly sliding the plates inward and outward, AC current will be generated in the external circuit [24-25].

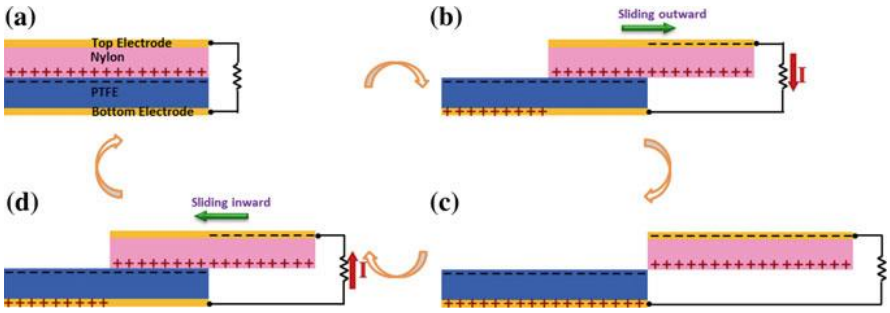


**Figure 2.1 Schematic of TENG working in lateral sliding mode [24]. Copyright 2013. Reproduced with permission from American Chemical Society.**

### 2.1.3 Single Electrode Mode

The main drawback of the last two mentioned modes is that not only they both need two electrodes, but also they require a mobile system. Single electrode mode suggests a configuration of TENG that can convert mechanical energy to electrical energy by using only one electrode [3]. Single electrode mode includes one electrode attached to one moving dielectric and it can exchange electrons when touches another material (Figure 2.2). Same as contact and separation or lateral sliding mode, separation of opposite charges leads to potential difference and derive electrons from the reference electrode (Cu) in order to compensate the potential difference (Figure 2.2 (b and c)). When charged surfaces get in touch again, the potential difference will be removed and electrons will flow back to their original position (Figure 2.2 (d)). Thus, an AC current generates as a result of contact and separation of opposite charges [26-27]. It is worth mentioning that single electrode mode can work in both forms of contact separation mode or lateral sliding mode [28].

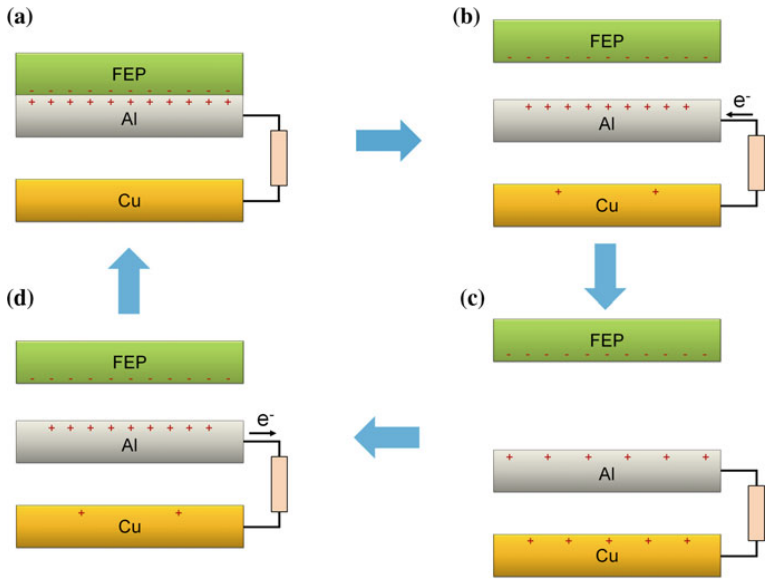


**Figure 2.2 Working mechanism of TENG in single electrode mode [3]. With copyright permission.**

### 2.1.4 Free-standing TENG Layer Mode

Free-standing layer is another working mode for TENGs. Figure 2.3 displays the free-standing layer mechanism. In this mode, two electrodes get in contact with a moving dielectric surface with completely different triboelectric properties. When the dielectric exchanges charges with the first electrode, the system is in equilibrium (Figure 2.3 (i)). In contrast, by moving the charged dielectric surface toward the other electrode, a potential difference derives electrons from one electrode to the other in an external circuit (Figure 2.3 (ii)). TENG system reaches equilibrium again when dielectric surface touches the second electrode completely and enough amount of electrons have been moved between electrodes (Figure 2.3 (iii)). In the last step, the dielectric plate slides back to get in touch with the first electrode again and electrons flow back to their original position (Figure 2.3 (iv)) [29-30].

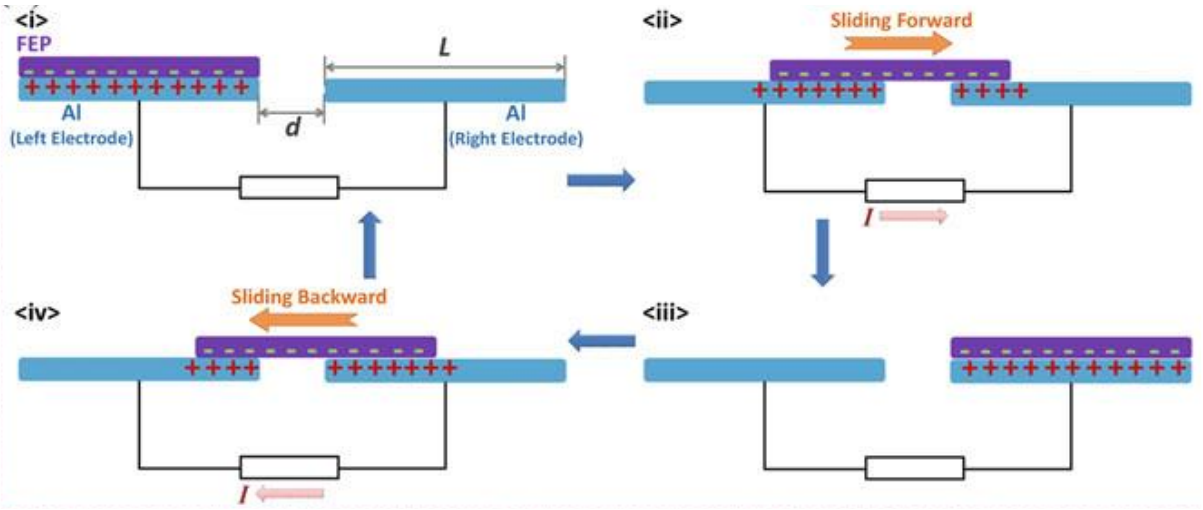


**Figure 2.3 Principal of free-standing layer schematic [29]. With copyright permission.**

## 2.2 Fundamental Theory of TENGs in Contact and Separation Mode

In general, contact and separation mode can be sub-divided into two categories: dielectric-dielectric type (Figure 2.4 (a)) or dielectric-conductor type (Figure 2.4 (b)).

As Figure 2.4 depicts, in the dielectric-dielectric contact and separation mode, two dielectric materials with thickness $d_1$ and $d_2$ and relative dielectric constant $\varepsilon_{r1}$ and $\varepsilon_{r2}$ are kept in touch. While they exchange electrons, the charge density of dielectric surfaces changes to $\sigma$ and $-\sigma$.

Furthermore, the air gap (distance) between two dielectrics is x(t), where t is time, and the amount of transferred charge between the two electrodes is Q.

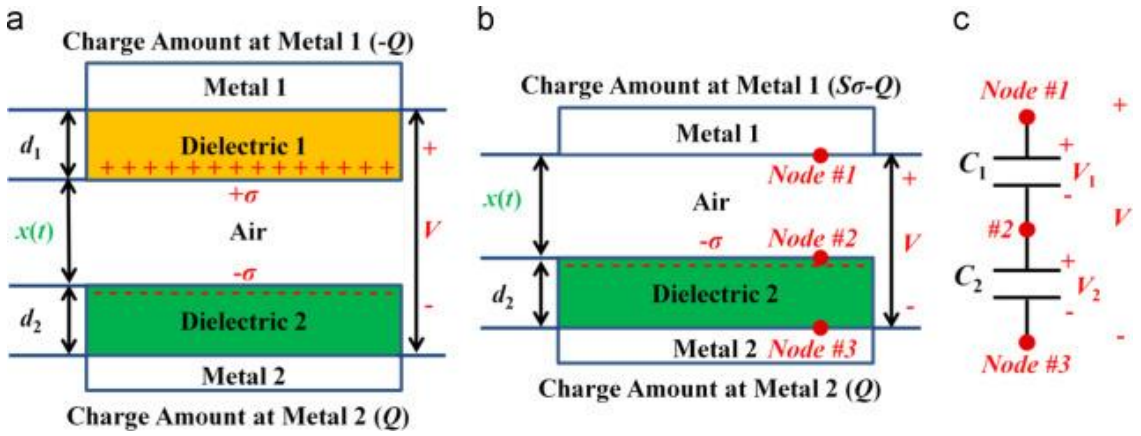


**Figure 2.4 Theoretical models for TENG in contact and separation mode. (a) dielectric-dielectric material, (b) dielectric-conductor material and (c) from capacitor point of view [31]. With copyright permission.**

On the other hand, in the conductor-dielectric type, the top electrode acts both as the positive side of the friction layers and the electrode, simultaneously. The amount of charge on top electrode comes from triboelectrification is:

$$Q_{TE} = S\sigma \quad \text{(Eq. 2.1)}$$

At the same time, the transferred charge between the two electrodes is -Q. Therefore, the total charge on the top electrode is:

$$\text{Top electrode total charge} = S\sigma - Q \quad \text{(Eq. 2.2)}$$

The strength of the electric field from Gauss theorem for the first dielectric is:

$$E_1 = -\frac{Q}{S\,\varepsilon_0\varepsilon_{r1}} \quad \text{(Eq. 2.3)}$$

The strength of the electric field for the air gap is:

$$E_{air}= \frac{\frac{-Q}{S}}{\varepsilon_0} + \frac{\sigma}{\varepsilon_0} \quad \text{(Eq. 2.4)}$$

The strength of the electric field for the second dielectric is:

$$E_2= - \frac{Q}{S\,\varepsilon_0\varepsilon_{r2}} \quad \text{(Eq. 2.5)}$$

The voltage between the electrodes derived from Equation (2.4):

$$V= E_1d_1+ E_2d_2 + E_{air}x \quad \text{(Eq. 2.6)}$$

By substituting Equations 2.1, 2.2 and 2.3 into Equation 2.4, the V-Q-X relation can be found as below:

$$V= - \frac{Q}{S\varepsilon_0}\left(\frac{d_1}{\varepsilon_{r1}} + \frac{d_2}{\varepsilon_{r2}} + x(t)\right) + \frac{\sigma}{\varepsilon_0}x(t) \quad \text{(Eq. 2.7)}$$

For the conductor-dielectric type, the value of $d_1$ is zero. Thus, the voltage would be in the form of Equation 2.6:

$$V= E_1d_2 + E_{air}x \quad \text{(Eq. 2.8)}$$

The relation between V-Q-X can be given by [31]:

$$V= - \frac{Q}{S\varepsilon_0}\left(\frac{d_2}{\varepsilon_{r1}} + x(t)\right) + \frac{\sigma}{\varepsilon_0}x(t) \quad \text{(Eq. 2.9)}$$

The V-Q-X relation can be simplified if we define the effective thickness constant of all dielectrics between two conductive electrodes as following:

$$d_0 = \sum_{i=1}^{n} \frac{d_i}{\varepsilon_{ri}} \quad \text{(Eq. 2.10)}$$

where $d_i$ and $\varepsilon_{ri}$ are the thickness and the dielectric constant of $i^{th}$ dielectric between the two metallic electrodes, respectively. As a result, we can simplify V-Q-X relation to:

$$V = -\frac{Q}{S\varepsilon_0}\left(d_0 + x(t)\right) + \frac{\sigma}{\varepsilon_0}x(t) \quad \text{(Eq. 2.11)}$$

Moreover, the intrinsic output characterization such as the open circuit voltage ($V_{OC}$), the short circuit charge ($Q_{SC}$) and the TENG capacity can be given by:

$$V_{OC} = \frac{\sigma}{\varepsilon_0}x(t) \quad \text{(Eq. 2.12)}$$

$$Q_{SC} = \frac{S.\sigma}{d_0 + X(t)}x(t) \quad \text{(Eq. 2.13)}$$

$$C = \frac{\varepsilon_0 S}{d_0 + X(t)} \quad \text{(Eq. 2.14)}$$

From different aspects, TENG resembles a capacitor in terms of energy storage [16] and as Figure 2.4 (c) displays dielectric surfaces play the role of capacitor's plates. Combining of TENG as capacitor and electrostatic induction point of view can be another approach to derive V-Q-X relation.

In electrostatic induction, a node is defined as a surface or volume with the same electric potential. Through this definition, the top electrode can be considered as the first node. By assuming that the area of friction layers are infinite and the dielectric layers are all uniform, the surface of the dielectric can be considered as node 2. In addition, node 3 is the bottom electrode since it has a constant electric potential. Every two nodes are connected by electrical lines, which indeed correspond to a capacitor. It is worth mentioning that because the dielectric surface is hypothetically infinite, node 2 blocks the electrical line connection between nodes 1 and 3.

Consequently, from the capacitance point of view, in conductor-dielectric mode, TENG is equivalent to a circuit including two flat-panel capacitors of $C_1$ and $C_2$ (Figure 2.4 (c)) [31].

## 2.3 Progress in the Development of Triboelectric Materials

TENG's simplicity and flexibility to harvest wasted mechanical energy are astonishing, but the major drawback of TENG is the generation of high output voltage but low current density [32]. Moreover, theoretical models of TENG in former section revealed that charge density is the most important parameter on TENG's performance.

In general, researches that aim to enhance TENG's performance focus either on increasing TENG charge density or designing a novel configuration to harvest a special type of mechanical energy. In the next section, researches related to some parameters that directly affect charge density are reviewed.

### 2.3.1 Friction Layer Material

In TENG design criteria, material selection is one of the very first steps. Most of the known materials have triboelectric properties naturally. Triboelectric series is a simple table that aims to organize triboelectric materials based on their tendency to lose or gain electron. Different triboelectric series are presented in different references but none of them are quantified [3]. Table 2.1 represents a simple triboelectric series. When a material with a high tendency to lose electron (i.e., near the top of table) touches a material with a lower tendency to lose electron (i.e., near the bottom of table), they will be able to exchange more electrons because of their larger difference in triboelectric properties [33].

**Table 2.1 Triboelectric series following a tendency of easy losing electrons (positive) to gaining electrons (negative) [34].**

| Triboelectric series |
|---|
| Wool |
| Nylon |
| Viscose |
| Cotton |
| Silk |
| Acetate |
| Lucite |
| Poly(Vinyl alcohol) |
| Dacron |
| Velon |
| Polyethylene |
| Teflon |

### 2.3.2 Surface Treatment

Surface treatment includes all the modifications on the TENG friction layers in order to enhance charge generation and storage during their contact and separation [34]. Fabrication of surfaces with microstructure patterns or foam structures are two important methods in order to modify the friction layer surface.

Fan *et al.* studied the effect of different microstructure patterns on triboelectric performance. They fabricated PDMS (polydimethylsiloxane) film with line, cube and pyramid microstructure patterns and compared TENG output with non-patterned PDMS film. Figure 2.5 illustrates both voltage and current increased when the pattern changes from solid to line, cube and pyramid, respectively [15]. This can be attributed to the fact that friction layers with more complex surface structures led to higher triboelectric effect since the separation of triboelectric charges occurs easier in microstructured surfaces. Moreover, the presence of air voids improved the capacitance and

effective dielectric constant significantly. On the microstructured surfaces, triboelectric charges were more easily separated [15].

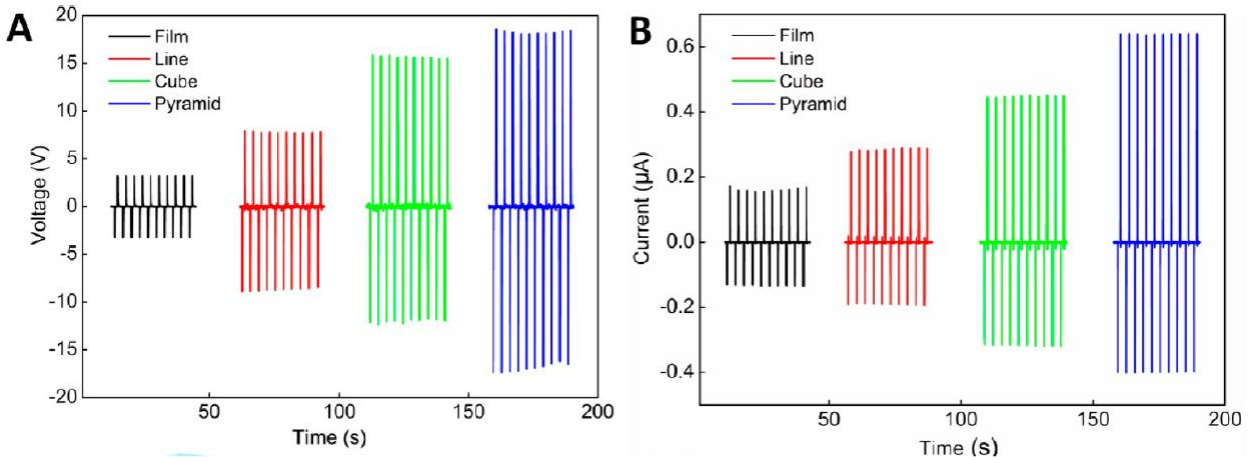


**Figure 2.5 Effect of microstructured friction layer on TENG output. (a) TENG output voltage and (b) TENG output current [15]. Copyright 2012. Reproduced with permission from American Chemical Society.**

Fabrication of foam structures in the friction layers is considered as another surface treatment method [35]. Indeed, foam structure provides higher surface area to volume ratio and consequently improves TENG charge density and performance. Lee *et al.* fabricated a hydrophobic sponge structure of PDMS and investigated the effect of different pore sizes in the friction layers on TENG performance. A piece of aluminum foil acted as the positive side of the friction layer and the electrode simultaneously. Figure 2.6 summarizes the output voltage of the fabricated TENG under various contact forces using PDMS foams with different pore sizes.

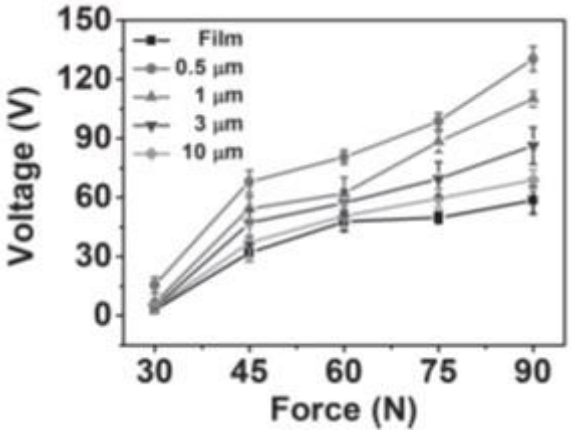


**Figure 2.6 Effect of PDMS porosity and contact force on TENG output voltage [13]. Copyright 2014. Reproduced with permission from Wiley Online Library.**

Figure 2.6 shows that the output voltage could be increased by either increasing the contact force or decreasing the PDMS pore size. With the sponge structure, the area to volume ratio increased when the pore size decreased. As a result, charge density and output voltage increased. Moreover, some extra charges generated on the surface of the inner pores, which contributed to the improvement of sponge-based TENGs performance [13]. Furthermore, a stronger contact force helped the effective contact area to reach its maximum value [36].

### 2.3.3 Chemical Treatment

In chemical treatment friction layer's triboelectric properties enhances by manipulating chemical composition or structure of material. Fabrication of high dielectric composites [37], fluorinated surfaces [38], ion injection [39], improvement of electroactive phase content count as part of the chemical treatment methods to enhance TENG performance [36], [40-41].

Chen *et al.* enhanced the performance of TENG by adding high dielectric nanoparticle fillers in PDMS sponge structure. $SiO_2$, $TiO_2$, $BaTiO_3$ and $SrTiO_3$ were used as high dielectric nanoparticles

with relative permittivity of 3, 80, 150 and 300, respectively. Figure 2.7 shows the effect of different fillers and the volume ratio of filler to PDMS on TENGs outputs [37].

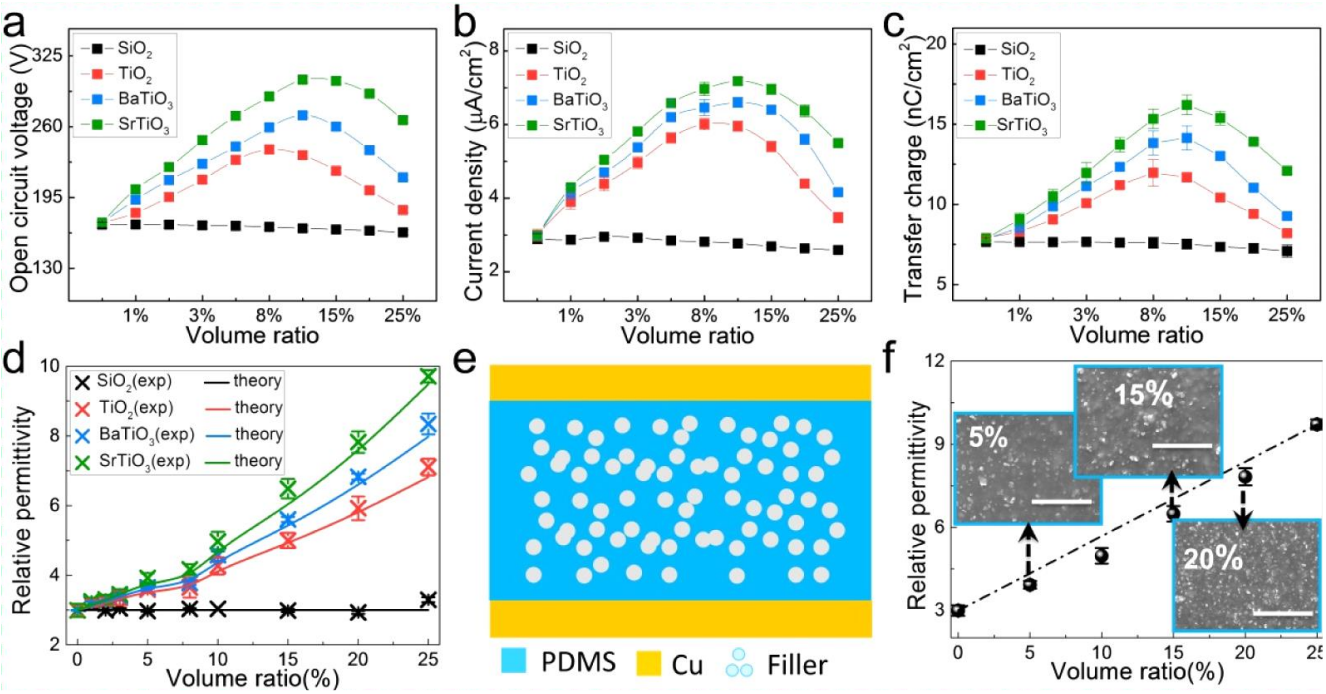


**Figure 2.7 Electrical measurements of the fabricated film based TENG (f = 2.5 Hz). (a) Open-circuit voltage, (b) short-current density, (c) amount of transferred charges, (d) comparison of relative permittivity of different matrixes, (e) schematic of composite films, (f) Relative permittivity changes as a function of SrTiO3 content from 0 to 25 vol %. The insets show SEM images of composite films at various volume ratios. The scale bars for SEM are 1 μm [37]. Copyright 2016. Reproduced with permission from American Chemical Society.**

Experimental observation revealed that the relative permittivity directly affects the electrical output of TENG. Increasing the dielectric constant of the composite would result in higher output voltage and current by the nanogenerator. It is worth mentioning that $SiO_2$ and PDMS have similar dielectric constant; thus, the addition of $SiO_2$ could not significantly change the TENG performance. Figure 2.7 (d) shows that the relative permittivity of composite followed Maxwell's equation and increased linearly by increasing volume ratio of filler in polymeric matrix [42]. In

contrast, the voltage and current density decreased when the volume ratio of filler was above 15%. This behavior attributed to the excess amount of filler particles appeared on the surface of PDMS which led to a decrease in PDMS effective area of friction layer [37].

Functionalizing the friction layer is another powerful tool to enhance TENG's efficiency. For instance, fluorine atoms have the highest electronegativity among all elements. Functionalizing the friction layer surface with fluorine atoms promotes the friction layer's tendency to attract electron during the contact and separation process. Shin *et al.* illustrated that polyethylene terephthalate (PET)-based nanogenerator output voltage was increased from 4 V to 330 V under the same conditions only by the addition of poly-$_L$-lysine and trichloro(1H,1H,2H,2H-perfluorooctyl) silane (FTOS) on the PET surface [38]. Since this method was complicated, another alternative method was to modify the friction layers that naturally have fluorine atoms in their structures. PVDF is one of these materials and has electroactive polymorphs (*i.e.* $\beta$ and $\gamma$) in its semi-crystalline structure. Increasing PVDF's electroactive phase content can enhance its ability to attract electron within contact and separation. Different methods are suggested to promote PVDF $\beta$ and $\gamma$ contents, which will discuss in the next section.

### 2.3.4 Promoting PVDF Electroactive Phase Content

#### 2.3.4.1 Mechanical Stretching

Stretching PVDF film at elevated temperature is one of the most commonly used approach that leads to a transformation of the $\alpha$ polymorphs to $\beta$ polymorphs. The applied stress by mechanical force allows the dipoles of PVDF chains to align normally to the direction of stress [9]. Under elevated temperature which optimally is 80℃, the mobility of PVDF chains increases and the higher mobility of chains would result in more transformations of $\alpha$ polymorphs to $\beta$ polymorphs.

It is worth mentioning that mechanical stretching can only turn a portion of $\alpha$ phase to $\beta$ phase and needs the application of heat and force simultaneously [43].

#### 2.3.4.2 Annealing

Transformation of $\alpha$ to $\beta$ can occur by exposing PVDF film to heat. It has been shown that higher mobility of PVDF chains at elevated temperature (80 to 115℃) is favorable to increase the $\beta$ phase content of PVDF. At a temperature lower than 80℃, chains mobility is insufficient for crystal transformation; however, at a temperature higher than 115℃, chain mobility is too high, which would lead to $\beta$ phase reverting back to $\alpha$ phase [44]. Moreover, it is reported that melting crystal structure at higher temperature (above 160℃) followed by slow cooling is favorable to promote $\gamma$ phase content of PVDF. Under these conditions, $\gamma$ polymorphs grow by using $\alpha$ crystal as seed [45-46].

#### 2.3.4.3 Fast Cooling

Quenching is a useful method to convert $\alpha$ polymorph to $\beta$ polymorph. Comparing to $\alpha$ polymorph, nucleation rate for $\beta$ phase can be promoted at lower temperatures. Therefore, the $\beta$ phase nucleation is dominant at lower temperature. At higher quenching rates, PVDF does not have the opportunity to form much of $\alpha$ polymorph. As a result, the formation of $\beta$ polymorph will be dominant [47].

#### 2.3.4.4 High Pressure

It has been proven that increasing the quenching pressure from 200 MPa to 700 MPa could promote $\beta$ phase content of sample from 0 to 100% and increasing the pressure to 800 MPa led to the formation of PVDF with 100% $\beta$ crystal [48].

### 2.3.4.5 Electrospinning

A simple fabrication method of PVDF with high electroactive phase content is electrospinning. As Figure 2.8 shows that electrospinning consists of three major components: high voltage supplier, metal collector and needle-syringe to provide feed [9].

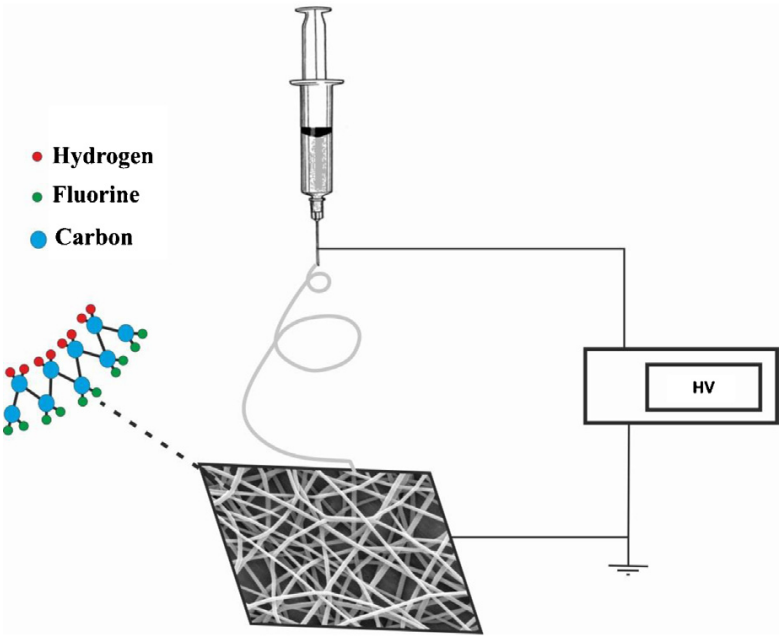


**Figure 2.8 Electrospinning setup for PVDF fabrication [9]. Copyright 2014. Reproduced with permission from Elsevier.**

In the electrospinning process, PVDF solution fills the syringe, which is being pushed by a syringe pump. Under a high voltage, solution droplets stretch and collect on the metallic collector. Flow rate, needle diameter, applied voltage and collector type are the most important parameters in electrospinning process. In general, $\beta$ phase of PVDF can be promoted by manipulation of electrospinning parameters in order to improve stretch of PVDF fibers [49].

#### 2.3.4.6 Electro-poling

Electro-poling uses the power of electric field to align dipoles along the electric field. In this method, an electrical field up to 100 MV/m was applied to the PVDF film for polarization [41]. This method is usually used as a post-treatment processing.

#### 2.3.4.7 Nanofillers

Some nanofillers have proven their abilities to promote $\beta$ or $\gamma$ content of PVDF by taking advantage of intermolecular interactions. Takur *et al.* revealed that remarkable improvement in PVDF $\beta$ phase up to 80% by making PVDF composite of $Ni(OH)_2$ nanobelt. The hydrogen bond between fluorine atoms of PVDF and –OH group of $Ni(OH)_2$ leads to alignment of PVDF chains on the surface of nanobelt and forms electroactive $\beta$ phase [50]. It is reported that $BaTiO_3$ ceramic filler can increase the β phase content of PVDF up to 80% only by the interaction between the local electric field around nanofiller and PVDF dipole [19]. On the other hand, KBr powder was used to promote the $\gamma$ phase content of PVDF. In an isothermal crystallization at 165℃ for 40 min, KBr acted as $\gamma$ phase nucleation agent. It was reported that KBr particle provides a crystallization surface for $\gamma$ polymorphs which must be attributed to the epitaxial growth of the γ-form PVDF crystallites on KBr surfaces [51].

### 2.4. Research Objectives

This research followed several short-term and minor objectives in order to satisfy its long-term objective. The main objective of this research was the development of a PVDF-based triboelectric nanogenerator with high triboelectrification and conversion efficiency. TENG with high conversion efficiency can be used as a reliable power source to run small electronic devices, particularly self-powered sensors.

Achievement to PVDF-based TENG with high conversion efficiency is impossible unless the effects of different design parameters on TENG performance have been elucidated. This was one of the short-term objectives of this research.

Geometric parameters such as the contact area and the thickness of friction layers were investigated as an effective parameter on TENG output signals. Moreover, PVDF porous structures with different pore sizes were fabricated to study the effects of the surface areas of friction layers on the TENG performance. In the second phase, non-isothermal crystallization and supercritical $CO_2$ processing followed by electro-poling were used to promote electroactive phase content of PVDF and then the effect of electroactive phase content on TENG performance was studied.

In the last phase, the influence of electrospinning process and chitin, PVDF-based friction layer were studied in order to increase the electrical output of TENG.

A better understanding of these effective parameters helps to optimize TENG design and improve the efficiency of energy conversion.

# Chapter 3 Geometrical and Morphological Parameters

This chapter mainly discusses the effects of geometry (*i.e.*, contact area and thickness) and morphology on triboelectrification. Compression molding process and salt leaching process were used to fabricate PVDF solid and open cell films, respectively. Different PVDF morphologies were studied after salt leaching process to comprehensively elucidate the effect of pore size and porosity on triboelectrification.

## 3.1 Experimental

### 3.1.1 Material

PVDF (Kynar 741, Arkema) in powder form was used to fabricate all the PVDF samples. Commercial sodium chloride (NaCl) was used as leaching agent. Table 3.1 shows the physical properties of materials. Copper tape with conductive adhesive on one side was used as negative side electrode. Commercial aluminum foil acted as positive side of TENG friction layer and electrode at same time and double-sided tape attached electrodes to the TENG substrate plates. All the materials were used without further modification.

**Table 3.1 Physical properties of PVDF and NaCl**

| Material | Melting Temperature (℃) | Density ($g/cm^3$) |
|---|---|---|
| PVDF | 168 | 1.78 |
| NaCl | 901 | 2.16 |

### 3.1.2 Solid Film Preparation

PVDF solid films were fabricated by compression molding machine (Craver Press, 4386 CH). Based on PVDF density and volume of molds, proper amount of PVDF was loaded into molds with different thicknesses (*i.e.*, 0.55, 0.22 and 0.15 mm). Each mold was held between compression molding machine plates for 5 minutes at 185℃ to ensure complete melting of PVDF powder and then compression molding pressure ramped to 10000 $lb_f$ for another 5 minutes at the same temperature. Subsequently, molds were cooled down and cut into rectangular shapes with different contact areas (*i.e.*, 2, 4, 6 and 8 $cm^2$).

### 3.1.3 Open Cell Foam Preparation

Open cell structures of PVDF were fabricated by combining compression molding and salt leaching process. The procedure can be described in 5 consecutive steps:

**Step 1.** NaCl particles were sieved into different size ranges (*i.e.*, <53, 53-106, 106-250 and 250-500 μm).

**Step 2.** PVDF powder was dry-blended with 80 wt.% NaCl powders.

**Step 3.** The mixture of PVDF and NaCl were loaded to molds (diameter 2 cm and thickness 0.5 mm) and compression molding process followed similar to solid film's preparation at 185℃ and 10000 $lb_f$.

**Step 4.** All the samples were submerged in water for 72 hours to leach out all the NaCl salt particles through structure. Water was changed with fresh water daily in order to avoid saturation with salt. Figure 3.1 shows PVDF samples before and after leaching out the salt particles.

**Step 5.** The open cell PVDF foams were dried overnight in a vacuumed oven at 60℃ to remove trapped water inside structure.

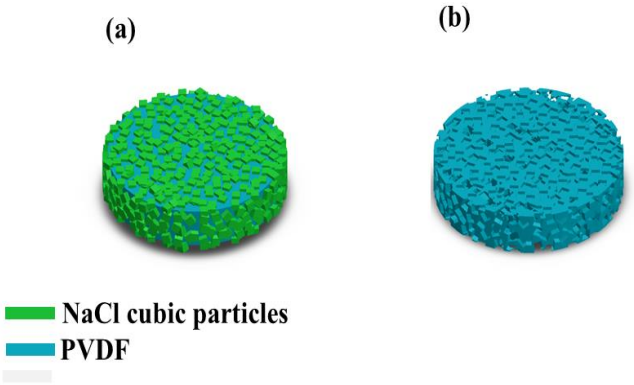


**Figure 3.1 Schematic diagram of the open cell foam structure of PVDF. (a) Before leaching out NaCl particles, and (b) after leaching out salt.**

Table 3.2 summarizes all the prepared PVDF based friction layers and their particular geometrical and morphological characterization.

**Table 3.2 Characterization of prepared PVDF based friction layer**

| Film type | Material | Thickness (mm) | Contact area ($cm^2$) | Pore size (µm) | Shape |
|---|---|---|---|---|---|
| Solid | PVDF | 0.15, 0.22 and 0.55 | 2, 4, 6 and 8 | - | Rectangular |
| Open cell | PVDF | 0.55 | 3.14 | <53<br>53-106<br>106-250<br>250-500 | Circular |

### 3.1.4 TENG Design

TENG was tested in the contact and separation mode. Figure 3.2 displays a schematic of the TENG device which was used over this chapter. Two acrylic plates (side length 9cm × 13cm) were used as the top and bottom substrates. Copper tape was used as the negative side electrode and different sizes of fabricated PVDF-based friction layer were attached to upper acrylic plate. Al foil was attached to the bottom plate. TENG friction layers and electrodes were mounted on substrate plates by using double-sided tape. 195 g weight was added to the top plate in order to increase the contact

force. Additionally, a rectifier comprising 4 diodes was used to convert AC current to DC current before electrical measurements. TENG output was measured while the top plate and attached weight were dropped on the bottom plate with a frequency of 3 Hz from a height of 3 cm.

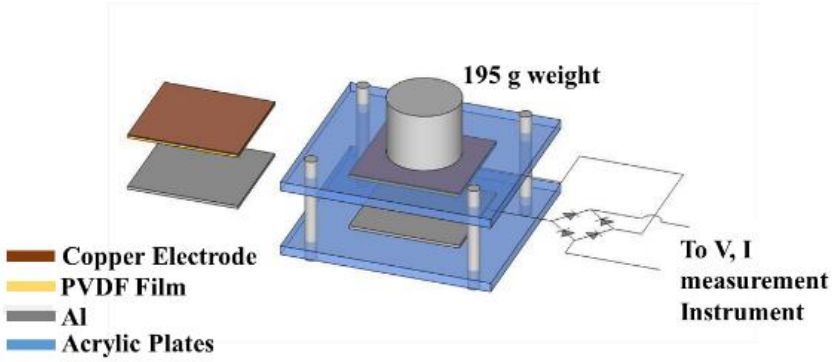


**Figure 3.2 Schematic design of TENG.**

## 3.2 Characterization

Scanning electron microscopy (SEM, Quanta 3D FEG, from FEI Company) was used to study PVDF foam structures. SEM micrographs of porous PVDF samples were taken after cryo-fracturing the samples under liquid nitrogen and then gold coating them with a sputter coater (Denton Vacuum, Desk V Sputter Coater). Open cell contents of open cell foams were investigated by a gas pycnometer (Quantachrome, Ultrapyc 1200e). The open cell content is defined as the percentage of interconnected cells with respect to the geometric volume of sample. Nitrogen gas was used to determine the total volume of the solid part and the closed cells ($V_t$) by employing Archimedes' principle of fluid displacement and Boyle's Law of gas expansion. Then, the open-cell content (porosity) determined by Equation (3.1).

$$\text{Porosity } \% = \frac{V_g - V_t}{V_g} \times 100 \qquad \text{(Eq. 3.1)}$$

where $V_g$ is the geometric volume of the foam sample.

The surface areas of foams were measured by Micro-CT scan (SKYSCAN 1272, BRUKER) and a Tektronix, TBS1052B-EDU digital oscilloscope and a Keithley 2450 source meter were used in order to measure open circuit voltage ($V_{oc}$) and short circuit current ($I_{sc}$) output of TENG, respectively.

## 3.3 Results and Discussion

### 3.3.1 Effect of Geometry (Thickness and Contact Area) on TENG Performance

PVDF solid films with different thicknesses (0.15, 0.22 and 0.55 mm) and contact areas (2, 4, 6 and 8 $cm^2$) were tested under the same conditions to elucidate the effect of geometry on TENG performance. For the positive side of friction layer, thin aluminum foil was used with the same contact area as the PVDF film. TENG open circuit voltage ($V_{OC}$) and short circuit current ($I_{SC}$) were measured by using an oscilloscope and a source meter, respectively. Data points were collected after 3 minutes of periodic contact and separation so that the friction layers would reach their maximum charge density capacity. The average of all $V_{OC}$ and $I_{SC}$ peaks were calculated and all tests were repeated by using 3 different samples under completely same conditions and the average in order to increase the reliability of results. The standard deviations were also reported. Figure 3.3 shows how the friction layer geometry affected both $V_{OC}$ and $I_{SC}$.

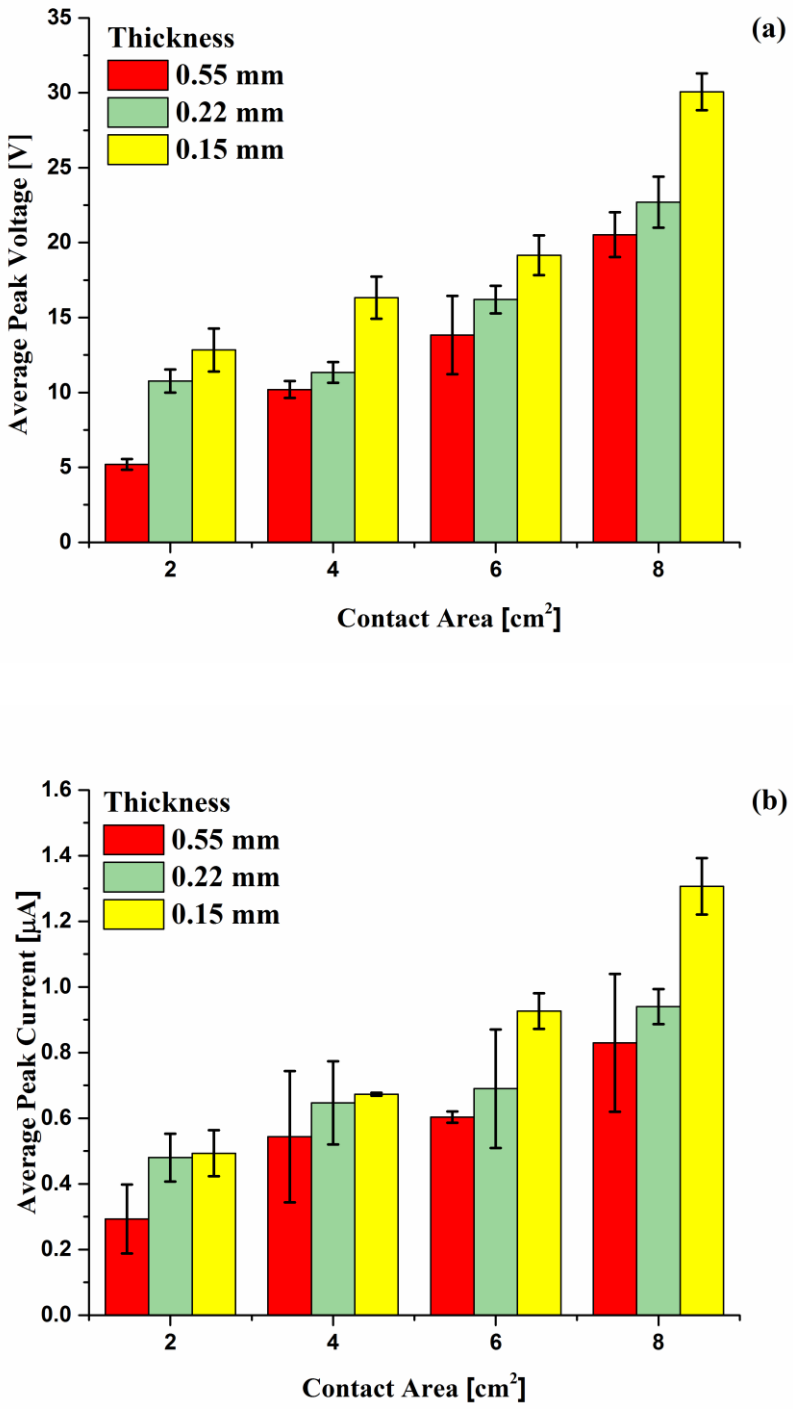


**Figure 3.3 Average of TENG output voltage and current using different thickness and contact area of solid PVDF as negative side of friction layer.**

Figure 3.3 illustrates that the geometry of the friction layer had a direct effect on TENG's electrical output. Increasing the contact area and at the same time decreasing the thickness of the friction layer enhanced the TENG's performance. The bigger contact area of TENG's friction layer would accumulate more triboelectric charges on TENG's opposite layers and as a result led to higher triboelectrification, increasing the TENG output. The important point here is the unclear relation of contact area and TENG open circuit voltage. There is no evidence in references about the fundamentals behind the relation of contact area and TENG voltage. Equation 2.12 shows $V_{OC} = \frac{\sigma}{\varepsilon_0} x(t)$ while there is not any term related to contact area. Most papers assume as contact area increases the capacity will increase but the relationship between the capacitance of friction layer and surface charge density is needed to be elucidated [16].

Moreover, output signals interpretation shows that a thinner friction layer enhanced both averages of voltage and current peaks, simultaneously. This can be attributed to two major reasons: first, thinner friction layer possesses a higher degree of electrostatic induction of triboelectric charges on electrode. Analytical correlation derived by Wang *et al*. confirms that friction layer's thickness (d) has a reverse effect on the induced charge density ($\sigma'$) on electrodes. Equation 3.2 can be used to describe this correlation between induced charge density and friction layer parameters:

$$\sigma' = \frac{\sigma.\ x(t)\ .\ \varepsilon_{r1}}{d_1.\varepsilon_{r1} + x(t)\varepsilon_{r1}} \qquad \text{(Eq. 3.2)}$$

where $\sigma'$ is the induced charge density; $\sigma$ is the triboelectric charge density, $\varepsilon_{r1}$ is the relative permittivity of negative side of triboelectric layer and $d_1$ and x(t) are the thickness of negative triboelectric layer and air gap, respectively [52].

Secondly, TENG can act as a storage device and an output device, simultaneously. TENG resembles flat-panel capacitors. Figure 3.4 shows that the equivalent capacitor schematic of a TENG. TENG in dielectric-conductor mode consists of two capacitors $C_1$ and $C_2$.

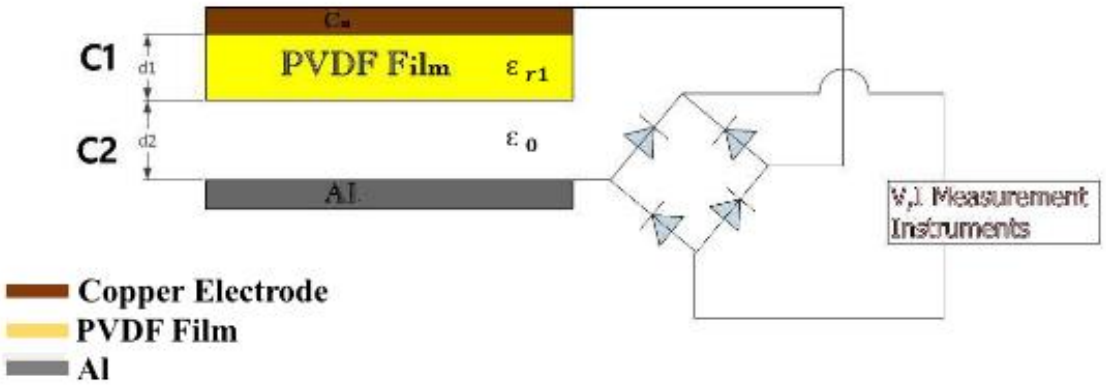


**Figure 3.4 Capacitor circuit schematic of a TENG.**

Essentially, the surface of the PVDF friction layer and the attached electrode played the role of the first capacitor plate and the surface of the PVDF friction layer and the conductive friction layer acted as second capacitors plates. The first capacitor has the capacitance of:

$$C_1 = \frac{\varepsilon_0 \varepsilon_{r1} S}{d_1} \quad \text{(Eq. 3.3)}$$

and the capacitance of the second capacitor can be expressed as:

$$C_2 = \frac{\varepsilon_0 S}{x(t)} \quad \text{(Eq. 3.4)}$$

where $\varepsilon_{r1}$, S and $d_1$ are the relative permittivity, contact area and thickness of the PVDF film, respectively, while $\varepsilon_0$ represents the dielectric constant of air and x(t) is air gap [16].

Based on the capacitance equations, thinner films would have a better ability to store charge and would consequently possess higher charge density. These would enhance TENG's output signals and power generation.

### 3.3.2 Effect of Morphology (Porosity) on TENG Performance

Open cell foam structures of PVDF with different pore sizes (*i.e.*, <53, 53-106, 106-250 and 250-500 μm) were fabricated using the salt leaching process. Figure 3.5 shows the SEM micrographs of fabricated samples prepared by salt particles of different sizes using the salt leaching approach.

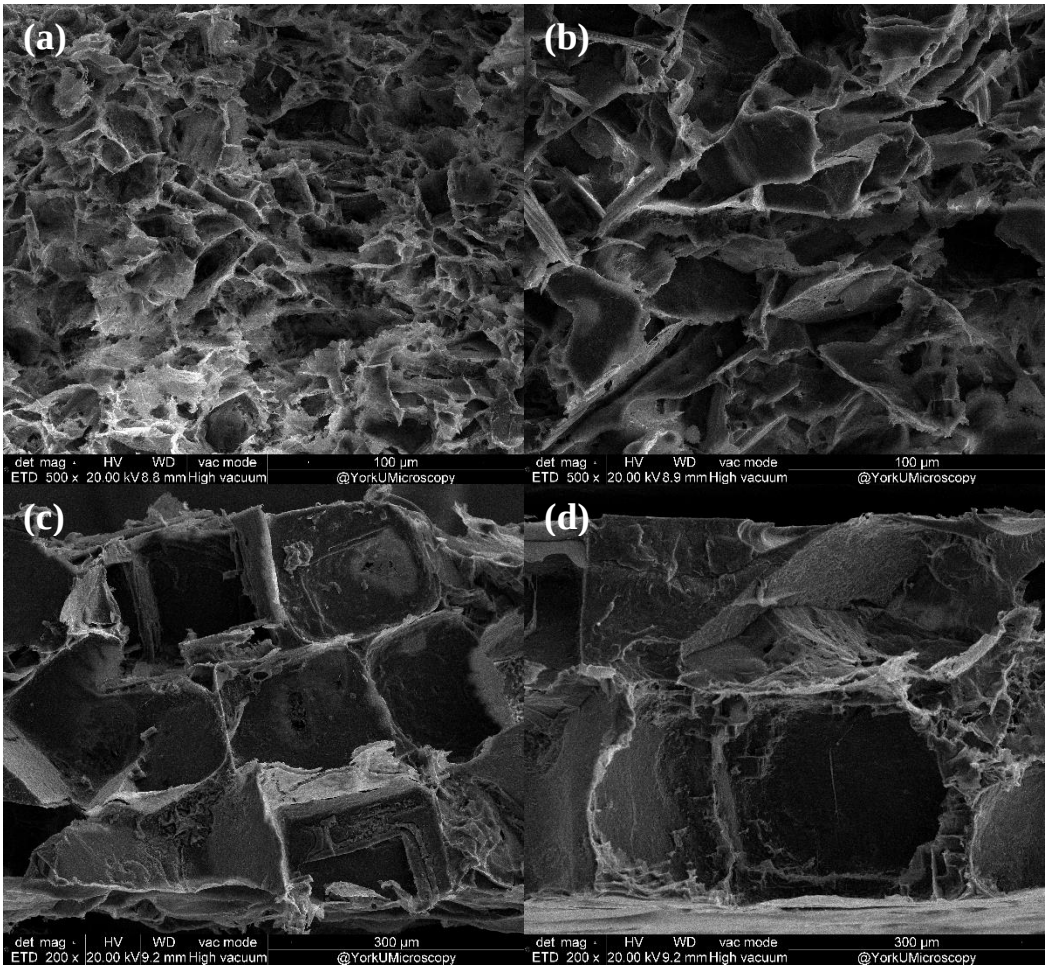


**Figure 3.5 SEM cross-section images of open cell samples prepared with different salt particle size of (a) <53, (b) 53-106, (c) 106-250 and (d) 250-500 μm.**

SEM micrographs revealed that PVDF foams had open cell structures and the sizes of pores almost corresponded to the sizes of the salt particles which were used in the fabrication process. Additionally, SEM images and weight of samples before and after salt leaching confirmed that all the salt particles had been removed by water. Pycnometer was used to measure the open cell content of samples and the results plotted in Figure 3.6 shows that samples possessed around 75% interconnected cells in their structures.

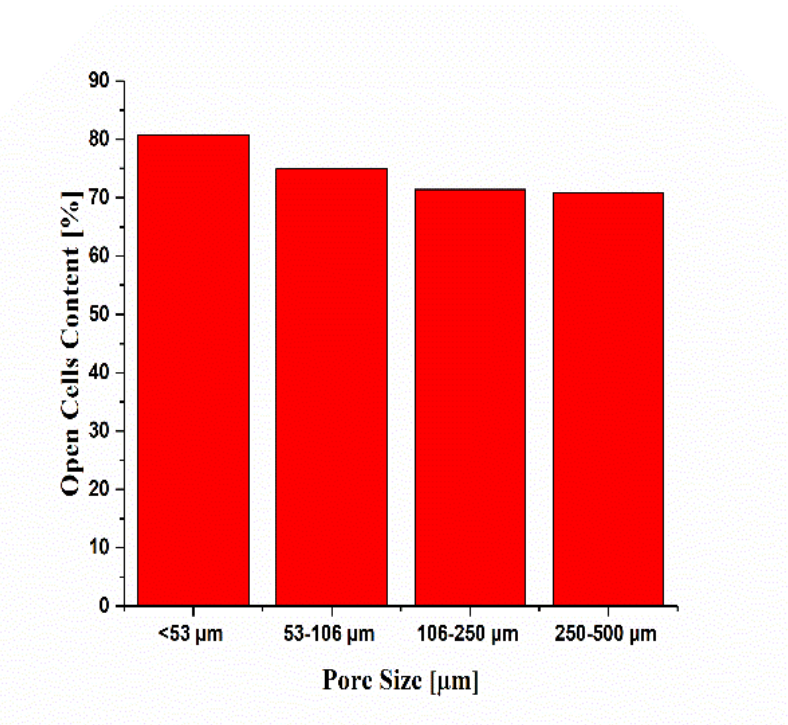


**Figure 3.6 Open cell content of PVDF foams prepared by salt leaching process.**

TENG output electrical signals were measured using open cell foams against Al foil. All experiments repeated in three batches with the same samples and under the same conditions. Figure 3.7 displays the average output voltage and current density peaks and their corresponding standard deviations.

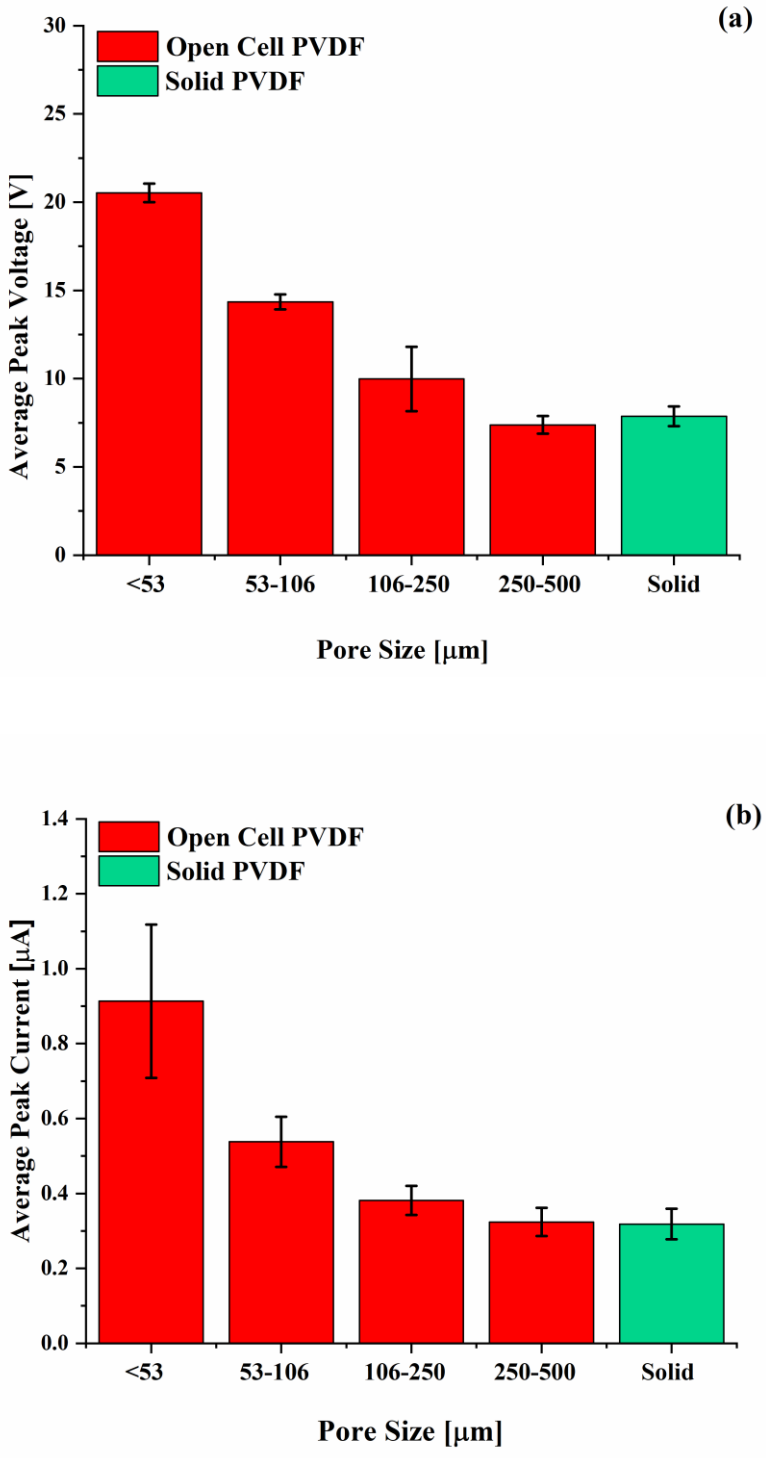


**Figure 3.7 Effect of pore size and open cell structure of PVDF foam on TENG outputs. (a) Average of output voltage and (b) average of current density peaks.**

TENG outputs revealed that introduction of pores into PVDF structure significantly improved the electrical output of the nanogenerator. On the other hand, it should be mentioned that nanogenerator outputs enhanced by decreasing the average pore sizes. The enhancement of TENG output was mainly caused by an increase in the surface area to volume ratio of the foam structure of the friction layers. The higher surface area of the friction layer improved the triboelectrification by increasing the contact area. Moreover, micro-CT scan in Figure 3.8 shows that foams prepared with the smallest salt particles (*i.e.*, <53 μm) had 5 times more surface area than prepared foam with bigger salt particles (*i.e.*, 250-500 μm). This confirms that smaller pores were able to provide higher contact area and to increase triboelectrification.

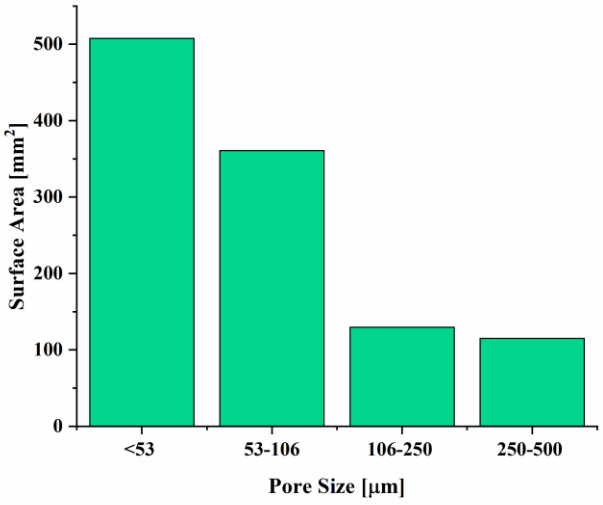


**Figure 3.8 Micro-CT scan results for surface area of fabricated open cell foams.**

Besides, foams were flexible, which means that under the contact force, friction layer would be compressed. As mentioned in the former section, thinner friction layer is able to generate higher charge density on the friction layer.

Output voltage and current were measured when different loads of resistors had been connected in the circuit in order to evaluate the TENG power density. Figure 3.9 shows the foam structure of PVDF with pore size smaller than 53 μm generated three times more power density when comparing to same size of solid PVDF. In addition, it is shown that the foam structure of PVDF with pores smaller than 53 μm could light up at least 30 serially connected commercial LEDs (Figure 3.9 (c)).

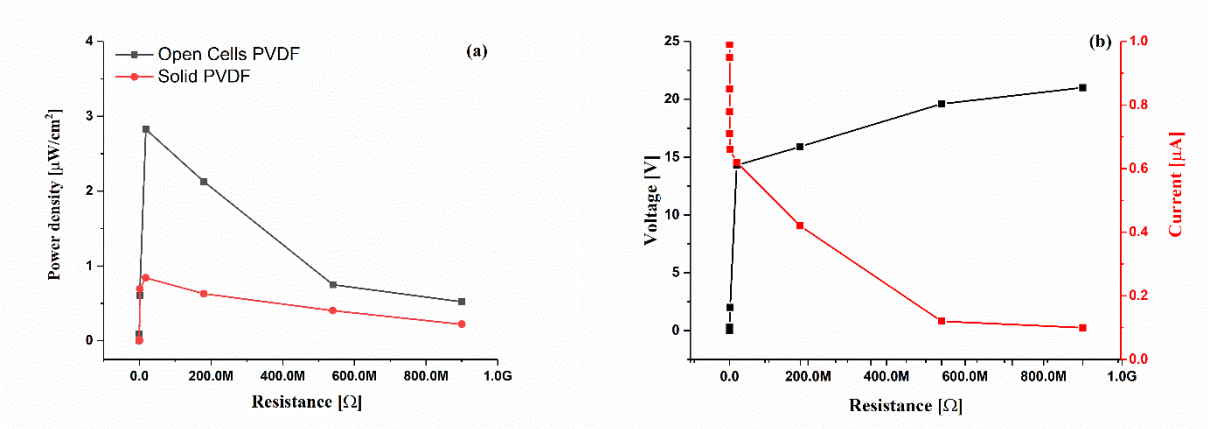


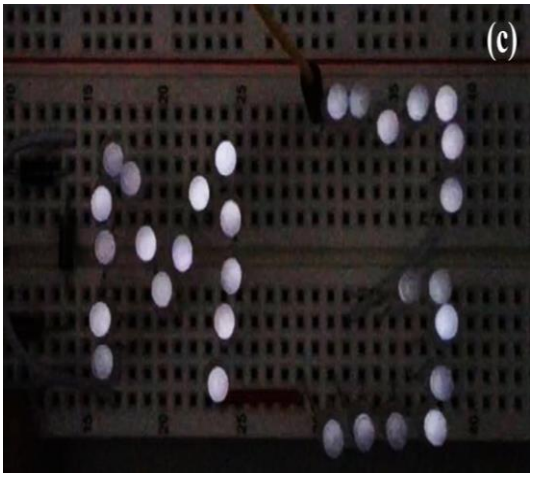


**Figure 3.9 TENG performance output. (a) Power density of TENG with open cell foam structure of PVDF (pore size less than 53 μm) and same size of solid PVDF. (b) Output voltage and output current of TENG with open cell foam structure of PVDF (pore size less than 53 μm) under variable load of resistors. (c) Digital photograph of LEDs running by TENG while open cell foam structure of PVDF (pore size less than 53 μm) was in use.**

## 3.4 Conclusion

In summary, PVDF solid films with different thicknesses and contact areas and PVDF open cell with different pore sizes were prepared to investigate the effects of geometry (*i.e.*, thickness and contact area) and morphology (*i.e.*, foam structure) of the friction layer on triboelectric nanogenerator (TENG) performance. Observations showed that TENG open circuit voltage ($V_{oc}$) and short circuit current ($I_{sc}$) increased either when the contact area of friction layer increased or its thickness decreased. The open circuit voltage and short circuit current changed from 5.2 V and 0.29 μA for solid PVDF film (2 $cm^2$ contact area and thickness 0.55 mm) to 30.1 V and 1.3 μA (for contact area of 8 $cm^2$ and thickness of 0.15 mm). Thinner film has a greater ability to induce electrostatic charges on electrode; therefore, TENG output was enhanced by decreasing friction layer thickness. Furthermore, a larger contact area would result in the accumulation of more charges on the dielectric surface, which could improve the TENG output. TENG electrical outputs for open cell foam structures of PVDF with different pore sizes were measured under the same operating conditions. The important point here is the unclear relation of contact area and TENG open circuit voltage. Most papers assume as contact area increases the capacity will increase but the relationship between the capacitance of friction layer and surface charge density is needed to be elucidated. The results showed that porous PVDF generated significantly more power during contact and separation. Moreover, it can be revealed that when the pore size decreased, both the open circuit voltage and the short circuit current increased. It could be attributed to the increased surface area to volume ratio in foam structures and compressible structure of foams, which led to the decrease in the friction layer thickness under applied mechanical force. Open cell PVDF foam structure with pore size less than 53 μm generated power density around 2.8 $\mu W/cm^2$, which was three times higher than the generated power density by same geometry of solid friction layer. In

order to evaluate the ability of TENG to operate electronic device, PVDF foam with pore size less than 53 μm was used to directly illuminate at least 30 commercial LEDs in series connection. This chapter gives a better understanding of the effects of geometrical and morphological structure of friction layer on the performance of the triboelectric nanogenerators and provides a novel way to enhance triboelectric output by tuning these parameters.

# Chapter 4 Electroactive Phase Content of PVDF and Triboelectrification

This chapter aims to elucidate the effect of PVDF electroactive phase content on triboelectrification. Supercritical $CO_2$ processing, non-isothermal crystallization and electro-poling were used to fabricate PVDF foams with high electroactive phase contents. The morphological and triboelectric properties of the fabricated samples were investigated.

## 4.1 Experimental

### 4.1.1 Materials

PVDF powder (Kynar 741, from Arkema) was used to prepare solid and foam samples of PVDF. Commercial aluminum foil was used as the positive side of the friction layer and at the same time as the positive electrode. Copper tape with conductive adhesive was used on one side as the negative electrode and double side tape was used in order to mount the electrodes on the substrates. Carbon dioxide ($CO_2$, purity 99.8%, Linde Gas Inc.) was used as the physical foaming agent and was pumped to a high pressure high temperature chamber. Commercial sodium chloride (NaCl) was used as the leaching agent to fabricate open cell PVDF foams. All materials were used as received without any further modification.

### 4.1.2 Solid Film Preparation

The compression molding process was used in order to fabricate solid PVDF films. First, proper amount of PVDF powder was loaded into mold (thickness 0.5 mm). Then, the mold was put into a compression molding machine (4386 CH, from Craver Press) preheated to 185 ℃. Compression molding machine's pressure on mold set to a negligible level until the temperature stabilized again at 185 ℃. Consequently, the compression pressure was ramped to 5000, 10000, 15000 $lb_f$ for 30

seconds in each step (*i.e.*, total 90 seconds). Finally, the heater was turned off and the mold was cooled down under a pressure of 15000 $lb_f$ for 8 hours.

### 4.1.3 Closed Cell PVDF Foam Preparation

Two different temperature profiles were considered for fabrication of PVDF foams in order to investigate their effects on promoting the PVDF's electroactive phase content. The first temperature profile was only about supercritical $CO_2$ ($ScCO_2$) processing. Here, solid PVDF films prepared by compression molding machine was cut into square pieces (side length of 0.5 inches) and enclosed into a high pressure high temperature chamber. The chamber was then heated up to the saturation temperature (*i.e.,* 160 ℃). Once the chamber had reached the saturation temperature, $CO_2$ was injected into the chamber at 2000 psi for 15 minutes using a syringe pump. After 15 minutes of subjecting the sample under the supercritical $CO_2$ environment, the gas was released by opening the outlet valve. Finally, the foamed PVDF sample was taken out and submerged into an ice bath to quench its microstructures. In the rest of this chapter, we will refer to this process as temperature profile one.

In the second temperature profile, the effects of non-isothermal crystallization and supercritical $CO_2$ processing on PVDF morphology and the sample's electroactive content had been investigated. In this temperature profile, the square shape of solid PVDF (side length of 0.5 inches) was enclosed in the same high pressure high temperature chamber. The chamber temperature was ramped to heating temperature ($T_H$ =180 ℃) and heater setpoint temperature immediately changed to the saturation temperature (*i.e.,* 160 ℃). When the chamber temperature reached the saturation temperature, supercritical $CO_2$ was injected into the chamber for 15 minutes. Finally, the gas was released through opening the outlet valve. Finally, the sample was taken out and submerged into an ice bath. It should be mentioned that in the rest of this chapter this process will be referred as

temperature profile two. Figure 4.1 schematically shows temperature profiles one and two adopted during the fabrication of PVDF foams with high electroactive phase contents.

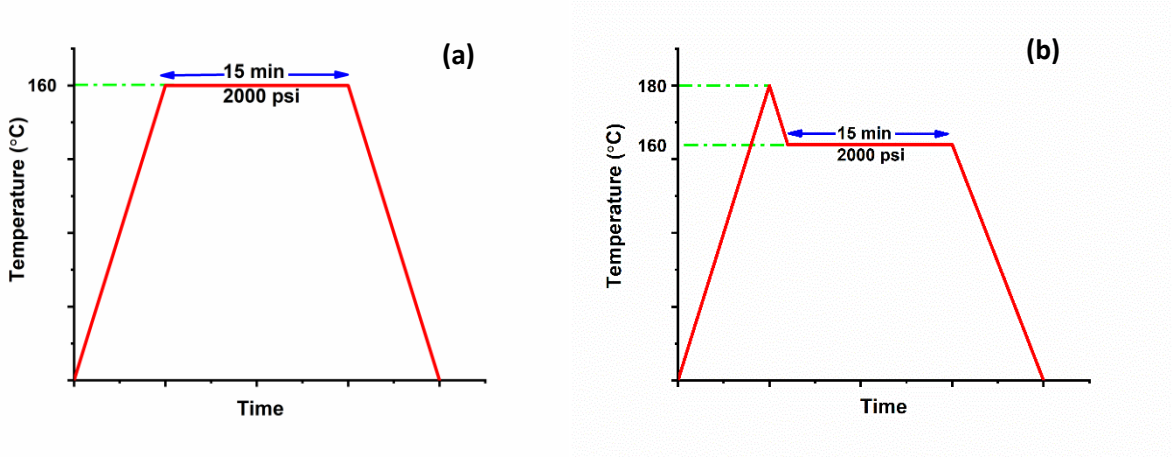


**Figure 4.1 Different processing conditions (*i.e.*, temperature, pressure and time). (a) Temperature profile one and (b) temperature profile two.**

The reason behind the selection of these two temperature profiles was based on Eun Lee *et al.* work, since they showed these two temperature profiles can be used to fabricate PVDF foam structure with even size of cells and high electroactive phase content [7], [57].

### 4.1.4 Preparation of Open Cell PVDF Foam with High Electroactive Content

The open cell structure of PVDF was fabricated by the salt leaching process (details were discussed in Chapter 3). The effects of non-isothermal crystallization and supercritical $CO_2$ processing (temperature profile two) was studied on open cell PVDF samples before leaching out the salt particles. At the end of process, samples were plunged into water for three days in order to leach salt particles out of structure.

Moreover, the effect of non-isothermal crystallization (temperature profile two) on PVDF solid samples was investigated. For this reason, temperature profile two had been applied to the solid samples without the injection of foaming agent ($CO_2$ gas) into the chamber.

### 4.1.5 TENG Design

In order to increase the contact force we changed the design to a hammer system. Here, triboelectric properties were tested by using contact and separation of a hammer. Hammer was connected to a rotating motor through gears. This provided enough energy for hammer's movement. Figure 4.2 shows the schematic of the hammer design to run TENG. TENG outputs were studied while the hammer and the mounted friction layer on it struck onto the Al foil on a fixed plate with a constant frequency of 1.3 Hz. Furthermore, a rectifier comprised of 4 diodes was used to convert AC to DC before electrical measurements.

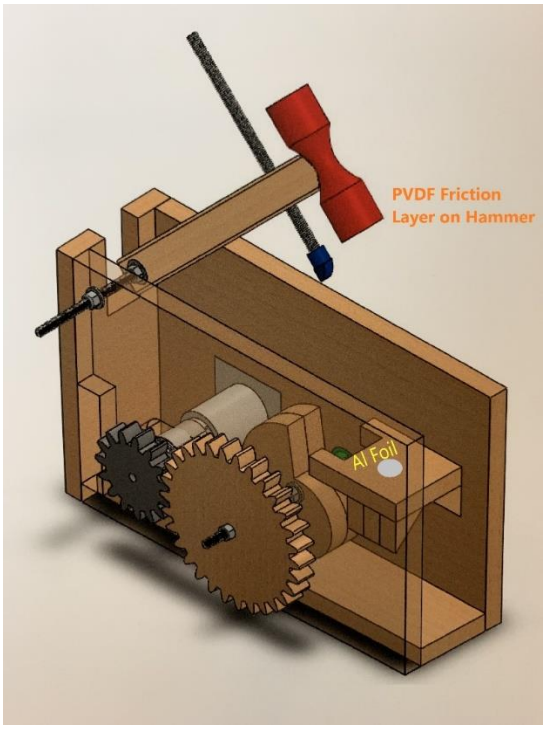


**Figure 4.2 Schematic of hammer design to run TENG.**

## 4.2 Characterization

In this section, we will review the methods which were used to characterize PVDF samples morphology and crystal structure.

### 4.2.1 Volume Expansion Ratio

Volume expansion ratio (VER) of foam samples was determined using the ASTM D792 standard. In this method, the weights of foam samples were measured in air and deionized water and VER was calculated by using equation 4.1:

$$VER = \frac{\rho\ (m_{air} - m_{water})}{m_{air}\ \rho_{water\ @\ T_w}} \quad \text{(Eq. 4.1)}$$

where $\rho$ is the density of PVDF powder (*i.e.*, 1.780 g.cm$^{-1}$), $m_{air}$ and $m_{water}$ are mass of samples in air and water, respectively, $T_w$ is temperature of water and $\rho_{water\ @\ Tw}$ is the density of water at $T_w$.

### 4.2.2 Scanning Electron Microscopy

Morphological properties of PVDF foam samples were characterized by using scanning electron microscopy (SEM, FEI Company Quanta 3D FEG). PVDF samples were cryo-fractured under liquid nitrogen and a gold layer was sputtered on them before taking the cross-sectional SEM micrographs. Additionally, SEM micrographs were further analyzed using ImageJ software to calculate the average of cell's size.

### 4.2.3 Fourier Transform Infrared Spectroscopy

Fourier transform infrared spectroscopy (FTIR, VERTEX 70/80, Bruker) was used to study PVDF polymorphs content. Number of scans was set to 24 with the resolution of 1 cm$^{-1}$ while wavenumber swept from 400 cm$^{-1}$ to 1500 cm$^{-1}$. Literature review shows that peak at 763 cm$^{-1}$ denotes to α phase and peak at 840 cm$^{-1}$ denotes to both $\beta$ and $\gamma$ [53-54]. $\beta$ and $\gamma$ phase were distinguished by peak to valley height ratio method suggested by Cai *et al.* [55]. Based on this method peaks at 763, 1234 and 1275 cm$^{-1}$ in PVDF's FTIR spectrum were related to $\alpha$, $\beta$ and $\gamma$, respectively, and the peak at 840 cm$^{-1}$ was related to both $\beta$ and $\gamma$. Obviously, for those samples

that did not have any peak at 1234 $cm^{-1}$ ($\gamma$ peak), peak at 840 $cm^{-1}$ was completely dedicated to $\beta$ phase and electroactive phase fraction will derive by using equation 4.2:

$$F_{EA} = \frac{A_{EA}}{1.26 \times A_{\alpha} + A_{EA}} \times 100\% \qquad \text{(Eq. 4.2)}$$

where $F_{EA}$ is the fraction of electroactive phase in PVDF samples which equals to $\beta$ phase content of samples, $A_{EA}$ and $A_{\alpha}$ are the absorbance band of the electroactive and $\alpha$ phase at 840 $cm^{-1}$ and 763 $cm^{-1}$, respectively.

For those samples that contained both peaks at 1234 $cm^{-1}$ and 1275 $cm^{-1}$ in their FTIR spectrum band (Figure 4.3), Equations (4.3) and (4.4) were used to calculate the β and γ phases contents separately.

$$F_{\beta} = F_{EA} \times \frac{\Delta H_{\beta}}{\Delta H_{\beta} + \Delta H_{\gamma}} \qquad \text{(Eq. 4.3)}$$

$$F_{\gamma} = F_{EA} \times \frac{\Delta H_{\gamma}}{\Delta H_{\beta} + \Delta H_{\gamma}} \qquad \text{(Eq. 4.4)}$$

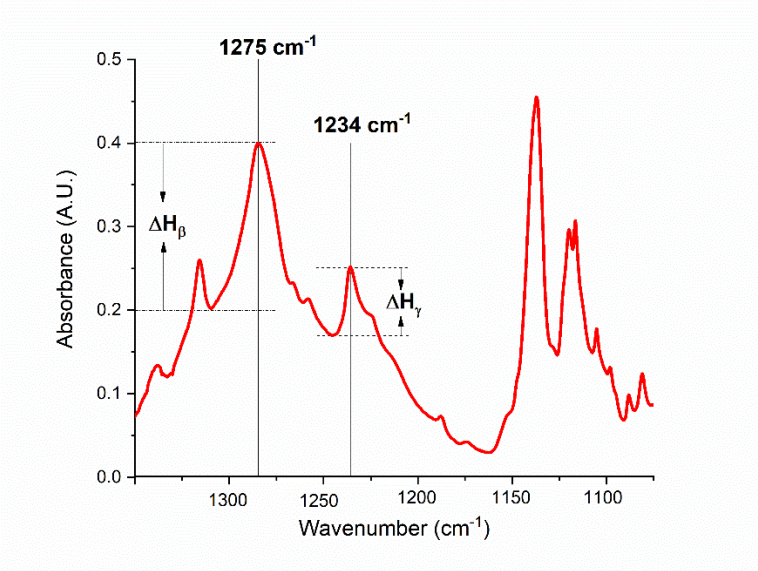


**Figure 4.3 Schematic of PVDF spectrum which contains both $\beta$ and $\gamma$ polymorphs in its semi-crystalline structure.**

where $F_\beta$ and $F_\gamma$ are the percentage fraction of $\beta$ and $\gamma$ polymorphs in PVDF crystal structure, $\Delta H_\beta$ and $\Delta H_\gamma$ are the height difference from the peaks at 1275 $cm^{-1}$ and 1234 $cm^{-1}$ to their nearest valleys, respectively.

### 4.2.4 Triboelectric Properties

Electrical outputs of TENG were measured by using a Tektronix digital oscilloscope (TBS1052B-EDU) and a Keithley 2450 source meter. TENG electrical outputs (i.e., open circuit voltage and short circuit current) were collected over 40 seconds and the average level of these peaks was calculated.

## 4.3 Results and Discussion

All measurements were repeated three times under the same conditions and the average of data points and their standard deviations were calculated. Moreover, all samples were dried overnight in a vacuumed oven at 60 ℃ before taking the electrical measurement to eliminate the effect of humidity on TENG outputs [56].

### 4.3.1 Effect of Temperature Profile One and Two on PVDF

FTIR was used to study PVDF polymorphs. Figure 4.4 shows the FTIR spectrum of PVDF samples. Figure 4.4 displays all the PVDF samples possessed peaks at 763 $cm^{-1}$ and 1275 $cm^{-1}$, which denoted the $\alpha$ and $\beta$ polymorphs, respectively. Moreover, it shows that the presence of electroactive phase peak at 840 $cm^{-1}$ in all samples, which denotes both $\beta$ and $\gamma$ phase, simultaneously. Most importantly, only the PVDF samples subjected to temperature profile two showed the γ peak at 1234 $cm^{-1}$.

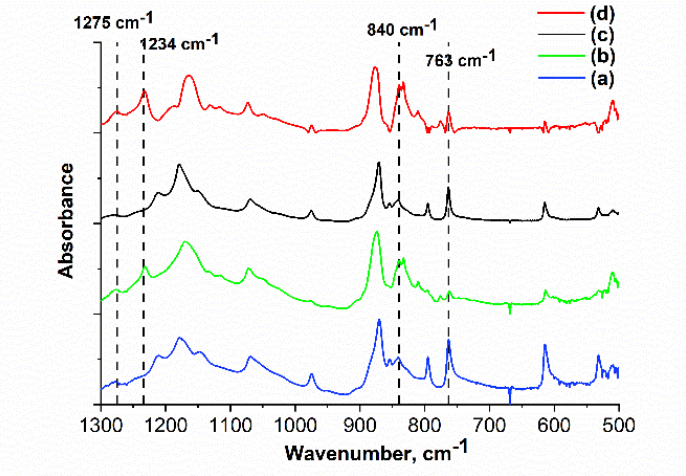


**Figure 4.4 FTIR spectra of prepared PVDF solid and foam samples: (a) solid PVDF sample prepared by compression molding; (b) solid PVDF sample subjected to temperature profile two without $CO_2$ injection; (c) foam PVDF after temperature profile one; and (d) foam PVDF after temperature profile two.**

In other words, non-isothermal crystallization was favorable for the growth of $\gamma$ phase polymorphs. This is mainly because at high temperatures $\alpha$ polymorphs melt and act as the seed for nucleation and growth of $\gamma$ polymorphs. FTIR data was further analyzed by using the peak to valley height ratio method and electroactive phase content (*i.e.,* $\beta$ and $\gamma$) of samples was calculated. Figure 4.5 shows that the electroactive phase content of PVDF samples, distinctively. Figure 4.5 reveals that temperature profile two significantly promoted the $\gamma$ phase content of samples up to 51%. Furthermore, it negatively affected the $\beta$ phase content of samples since $\beta$ content decreased from 36% to 10% and the key reason behind it was the compactness of $\gamma$ phase chains.

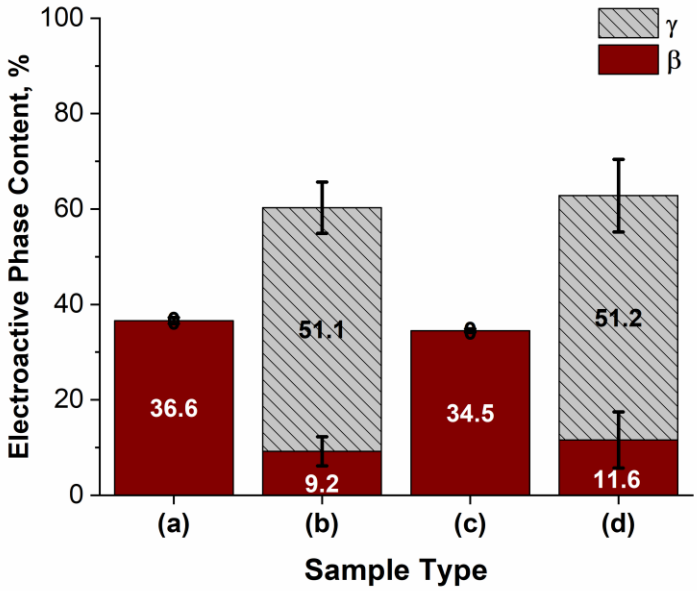


**Figure 4.5 Electroactive phase content of PVDF samples. (a) Solid PVDF sample prepared by compression molding process; (b) solid PVDF sample subjected to temperature profile two without $CO_2$ injection; (c) foam PVDF after temperature profile one; and (d) foam PVDF after temperature profile two.**

High compactness of $\gamma$ phase made it difficult for $CO_2$ molecules to diffuse into PVDF structure. As a result, PVDF foam would have a lower expansion rate, whereas, expansion of PVDF foam by $CO_2$ injection at elevated temperature mimicked mechanical stretching of PVDF chains which would be favorable to promote the $\beta$ phase content of PVDF. Thus, lower amounts of $\beta$ phase existed in samples with lower volume expansion ratio were expectable. Moreover, $\gamma$ phase growth was dominant over $\beta$ polymorph's growth in general [57].

Table 4.1 shows the VER of PVDF samples underwent both temperature profiles which confirms our observation and discussion about $\beta$ and $\gamma$ phase content of PVDF.

**Table 4.1 Volume expansion ratio**

| Sample type | VER |
|---|---|
| PVDF after $ScCO_2$ processing (temp. profile one) | 14 |
| PVDF after non-isothermal crystallization and $ScCO_2$ processing (temp. profile two) | 2.5 |

PVDF prepared using temperature profile two possessed much higher VER, which was caused by the promoted diffusion and expansion of foam by $CO_2$ molecules in the absence of $\gamma$ polymorphs.

Electrical outputs of TENG using solid and foam PVDF after both temperature profiles were measured under the same conditions and the results are shown in Figure 4.6. It should be mentioned that expanded foams were cold compressed overnight using a compression molding machine and mold with thickness of 0.5 mm to get rid of the effect of friction layer thickness on TENG electrical signals.

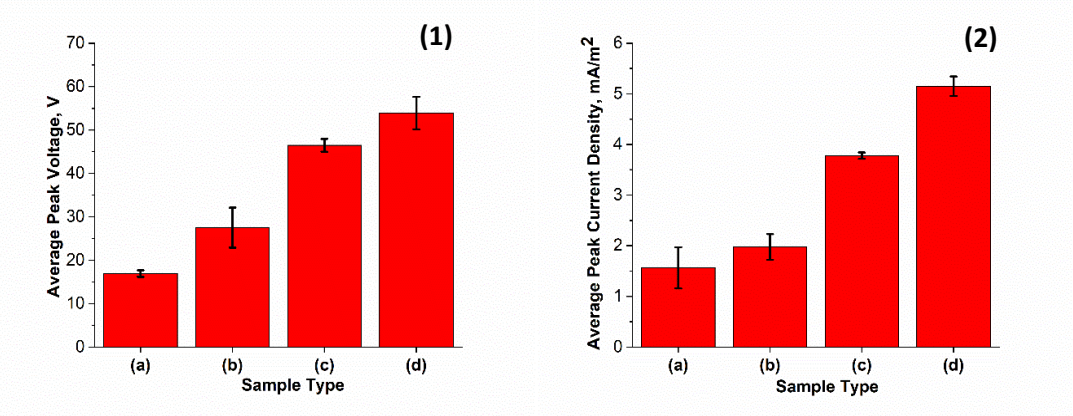


**Figure 4.6 Effect of non-isothermal crystallization and $ScCO_2$ processing on TENG electrical output. (1) Average of output voltage and (2) average of output current density. (a) Solid PVDF sample prepared by compression molding machine; (b) solid PVDF sample subjected to temperature profile two without $CO_2$ injection; (c) foam PVDF after temperature profile one; and (d) foam PVDF after temperature profile two.**

TENG outputs showed that temperature profile two greatly improved the average electrical signals. Temperature profile two increased the total electroactive phase content of PVDF by around 27%, which would result in an increase in the surface potential level of PVDF. Higher PVDF surface potential increased the difference between PVDF energy level and Al fermi level. This situation provided more room for electron transfer between dielectric and metal before they reached the same surface potential level and improved TENG electrical output [36].

On the other hand, SEM micrographs confirm that $CO_2$ injection led to the fabrication of porous structure (Figure 4.7).

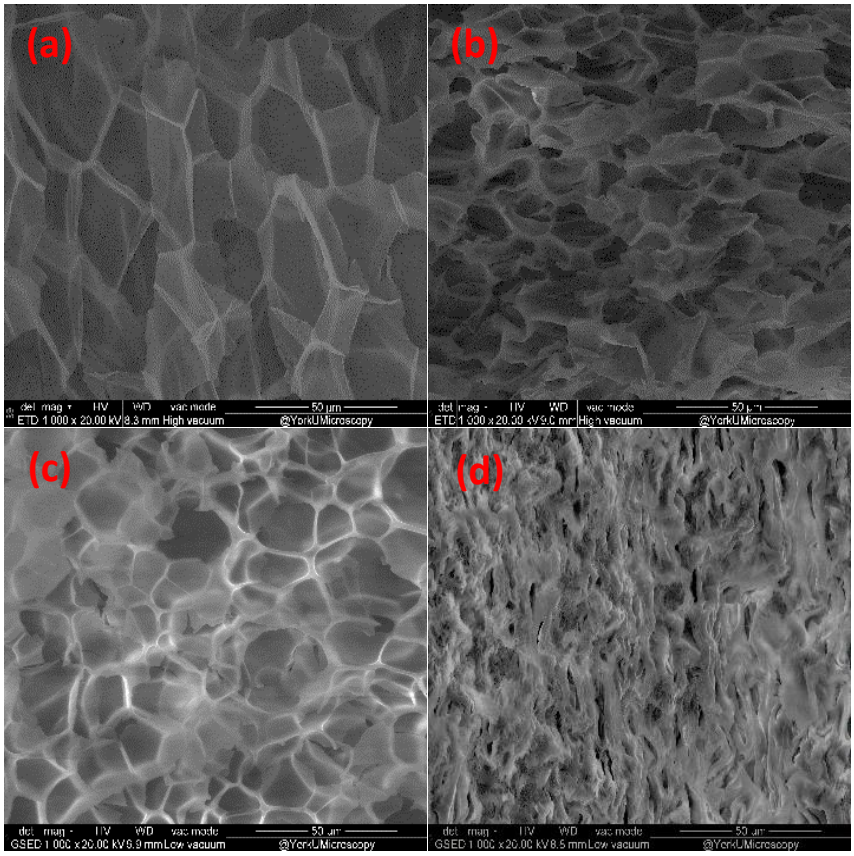


**Figure 4.7 SEM micrograph of PVDF. (a) PVDF foam after temperature profile one and before cold compression, (b) PVDF foam after temperature profile one and after cold compression, (c) PVDF foam after temperature profile two and before cold compression and (d) PVDF foam after temperature profile two and after cold compression.**

Moreover, ImageJ software was used to analyze the average pore size for both temperature profiles before and after cold compression and the results are shown in Table 4.2.

**Table 4.2 Cell diameters and standard deviations**

| Processing type | Average of cells diameter (μm) | Standard Deviation (μm) |
|---|---|---|
| Foam samples after temperature profile one before cold compression (VER= 14) | 11.7 | 3.9 |
| Foam samples after temperature profile two before cold compression (VER= 2.5) | 4.36 | 1.6 |
| Foam samples after temperature profile two and cold compression | 5.3 | 1.01 |
| Foam samples after temperature profile two and cold compression | 2.3 | 0.79 |

Injection of $CO_2$ gas at high pressure and elevated temperature introduced closed cell structure of pores into solid PVDF. Moreover, as shown in the SEM images of foams processed by temperature profile two, difficulty in $CO_2$ diffusion into the compact $\gamma$ chains resulted in lower cell expansion and consequently smaller pores size. As mentioned in Chapter 3, a porous friction layer possessed larger surface area and charge density would enhance TENG electrical signals. In summary, foam prepared using temperature profile two took advantage of both smaller pores size (*i.e.*, higher surface area) and higher content of electroactive polymorphs, which both would lead to generating more electricity in contact and separation.

Power density of PVDF films was calculated by using the prepared PVDF films as the negative side of friction layer. The voltage and current were measured when different loads of resistors were connected in circuit. Figure 4.8 depicts the power density output of TENG and again confirms

foam PVDF was able to generate the highest power density due to its porous structure and higher electroactive phase content.

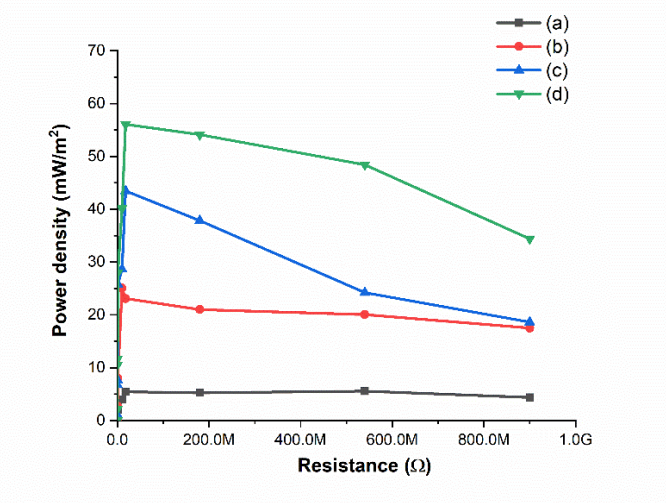


**Figure 4.8 Effect of porosity and EA content on TENG power density output. (a) Solid PVDF sample prepared by compression molding machine; (b) solid PVDF sample subjected to temperature profile two without $CO_2$ injection; (c) foam PVDF after temperature profile one; and (d) foam PVDF after temperature profile two.**

### 4.3.2 Effect of Electro-poling

Foam PVDF films were further modified by electro-poling method. In this method, the electroactive phase content of PVDF was enhanced through the exposure of the PVDF film to a strong electrical field. For this purpose, PVDF film was cold compressed under 15000 $lb_f$ using a compression molding machine overnight to make the films to be as thin as possible, Figure 4.9 shows the SEM micrographs of PVDF foams after cold compression.

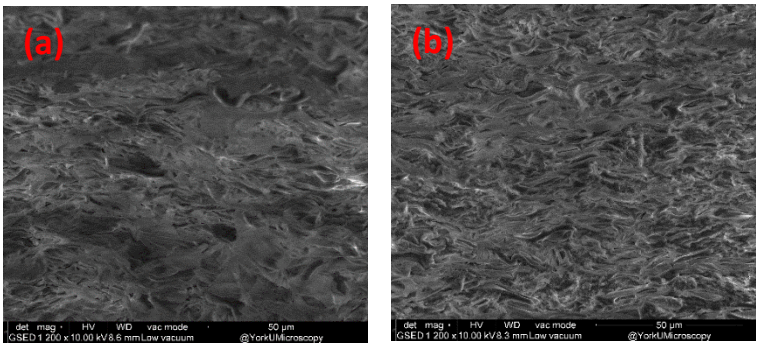


**Figure 4.9 SEM micrograph of porous PVDF after cold compression. (a) PVDF foam after temperature profile one and cold compression and (b) PVDF foam after temperature profile two and cold compression.**

For electro-poling, silver paste was applied as conductive electrode on both side of PVDF thin films and an electrical field of 0.07 kV/μm was applied for 30 minutes on the films using a high voltage power supply (Gamma High Voltage Research, Ormond Beach, FL). Eventually, the silver paste was peeled off and the electroactive phase content as well as the triboelectric properties of the films were analyzed.

FTIR analysis and the peak to valley height ratio method were used in order to measure the electroactive phase content of the PVDF samples after cold compression (*i.e.*, before electro-poling) and after electro-poling and the results are shown in Figure 4.10.

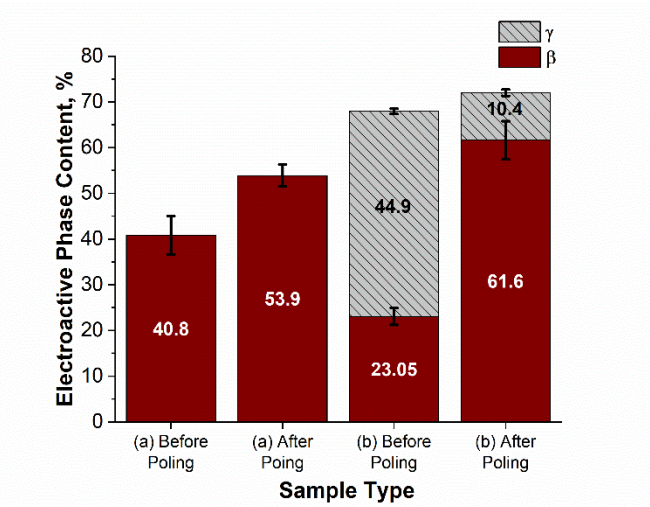


**Figure 4.10 Effect of cold compression and electro-poling on PVDF electroactive phase content. (a) PVDF foams processed by temperature profile one and (b) PVDF foam processed by temperature profile two.**

Figure 4.10 shows that cold compression slightly increased the $\beta$ phase content of PVDF. This was mainly because of mechanical stretch of PVDF film under compression molding high pressure [9]. $\beta$ phase content promoted significantly after electro-poling, which happens obviously because of the rearrangement of polymer chains across the electrical field. The effects of cold compression and electro-poling on TENG signals were studied under the same conditions and the results are displayed in Figure 4.11.

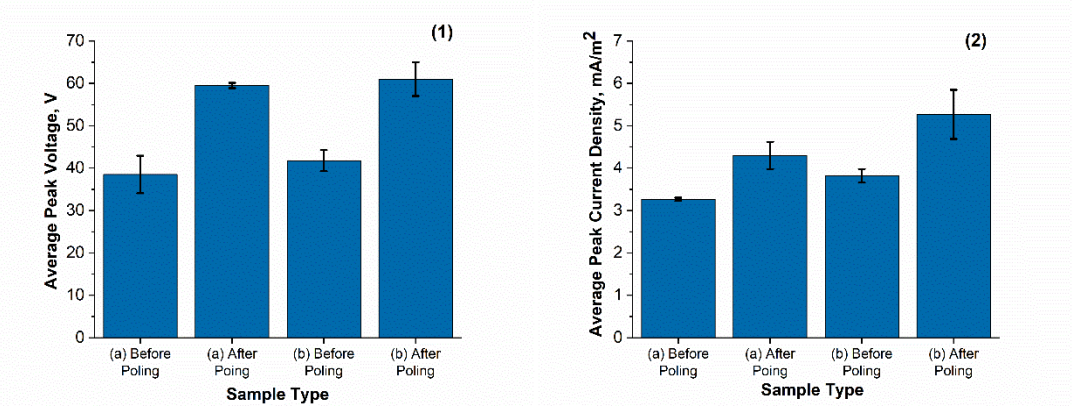


**Figure 4.11 Effect of cold compression and electro-poling on TENG outputs. (1) Average of output voltage and (2) average of current density. (a) PVDF foams processed by temperature profile one and (b) PVDF foam processed by temperature profile two.**

Figure 4.11 shows that the electrical output of TENG decreased after cold compression compared to the output results of same films before cold compression (Figure 4.6); however, friction layers were thinner with a higher content of electroactive phase. The weaker output signals could be attributed to the disruption of foam structure after cold compression and as a result foam flexibility was lost and the ratio of surface area to volume decreased. SEM micrographs in Figure 4.9 reveal the destruction of PVDF's porous structure.

Additionally, significant enhancement of PVDF $\beta$ phase content led to a surge in TENG output signals. This could be attributed to the greater opportunity of electron transfer between Al and PVDF based on their higher difference in work function after electro-poling.

### 4.3.3 Effect of Temperature Profile Two on Open Cell Structure of PVDF

Open cell structures of PVDF were prepared using the same method mentioned in Chapter 3. Nevertheless, before leaching out the salt particles, the samples had been subjected to temperature profile two in order to investigate the effects of non-isothermal crystallization and supercritical $CO_2$ processing on the open cell structures of PVDF foams. At the end of the temperature profile two, salt particles were leached out by submerging samples in water for three days and the PVDF foams were dried overnight in a vacuumed oven at 60 ℃.

FTIR and SEM were used to study the effect of temperature profile two on open cell PVDF's electroactive phase contents and microstructures, respectively. Figure 4.12 shows the electroactive phase contents of open cell PVDF before and after temperature profile two.

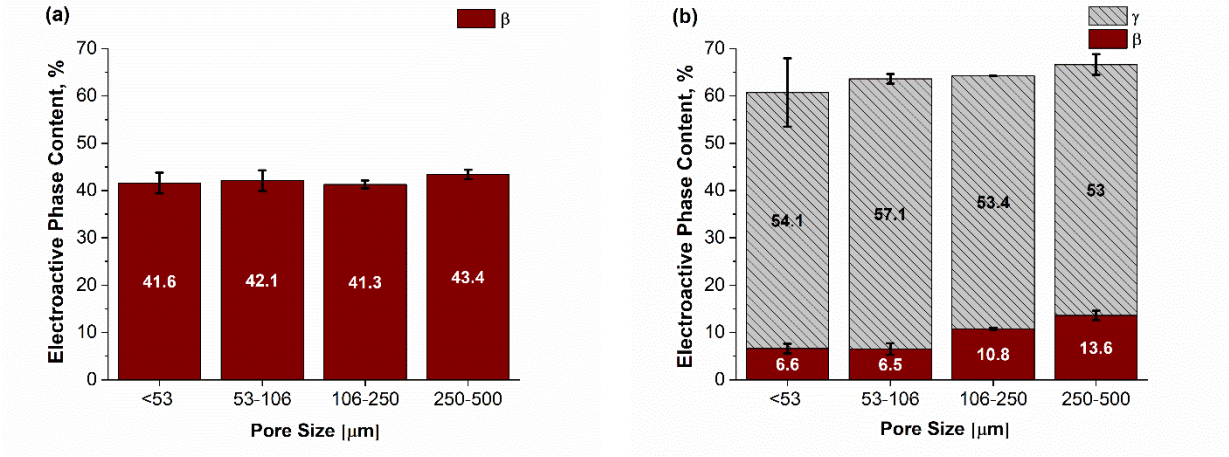


**Figure 4.12 Electroactive content of open cell structure of PVDF. (a) Before and (b) after processing under temperature profile two conditions.**

Figure 4.12 shows that the $\beta$ phase content of all open cell samples before undergoing temperature profile two was almost the same around 42%. After undergoing temperature profile two, their $\beta$ phase contents decreased significantly while $\gamma$ contents increased from 0% up to ~55%. This was mainly caused by the growth of $\gamma$ crystal by using the partially melted $\alpha$ polymorph as the

nucleation seeds. Furthermore, the compactness of $\gamma$ chains negatively affected the expansion of cells and growth of $\beta$ polymorphs.

Moreover, the triboelectric properties of open cell PVDF before and after processing under temperature profile two were studied. The average open circuit voltage and short circuit current density were measured and the results are shown in Figure 4.13.

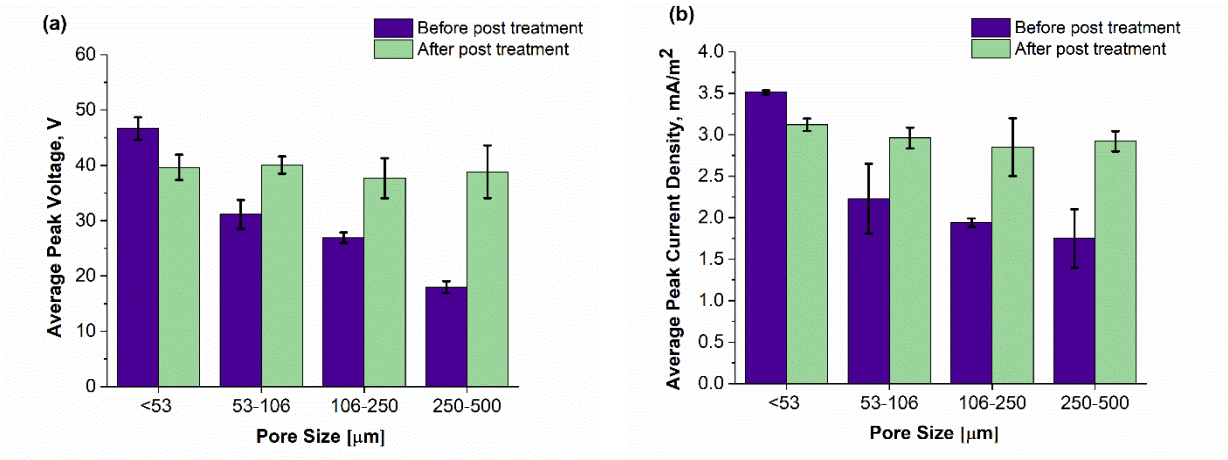


**Figure 4.13 Electrical output of TENG, using open cell PVDF before and after post-treatment (temperature profile two). (a) Average of voltage peaks and (b) average of current density peaks.**

The observations showed that after processing by temperature profile two, electrical outputs of all samples increased except the one with smallest pore sizes. (*i.e.*, <53 μm). On the other hand, SEM micrographs in Figure 4.14 show that temperature profile two led to a decrease in the average cell's size for all the samples except the one which prepared by salt particle size less than 53 μm. Thus, although for sample prepared with salt particle size less than 53 μm electroactive phase content is higher, lower electrical signals were observed because of the lower surface area and charge density. Table 4.3 summarizes the effect of temperature profile two on cell size.

**Table 4.3 Cell diameters and standard deviations**

| Sample Type | Average of cells diameter (μm) | Standard Deviation (μm) |
|---|---|---|
| Open cell after salt leaching (salt size less than 53 μm) | 4.7 | 3.9 |
| Open cell after salt leaching (salt size 53-106 μm) | 16.37 | 12.2 |
| Open cell after salt leaching (salt size 106-250 μm) | 43.68 | 68.5 |
| Open cell after salt leaching (salt size 250-500 μm) | 69.97 | 104.3 |
| Open cell after non-isothermal crystallization and $ScCO_2$ processing (salt size less than 53 μm) | 8.6 | 5.7 |
| Open cell after non-isothermal crystallization and $ScCO_2$ processing (salt size 53-106 μm) | 11.99 | 8.3 |
| Open cell after non-isothermal crystallization and $ScCO_2$ processing (salt size 106-250 μm) | 20.3 | 31.3 |
| Open cell after non-isothermal crystallization and $ScCO_2$ processing (salt size 250-500 μm) | 18.1 | 48.2 |

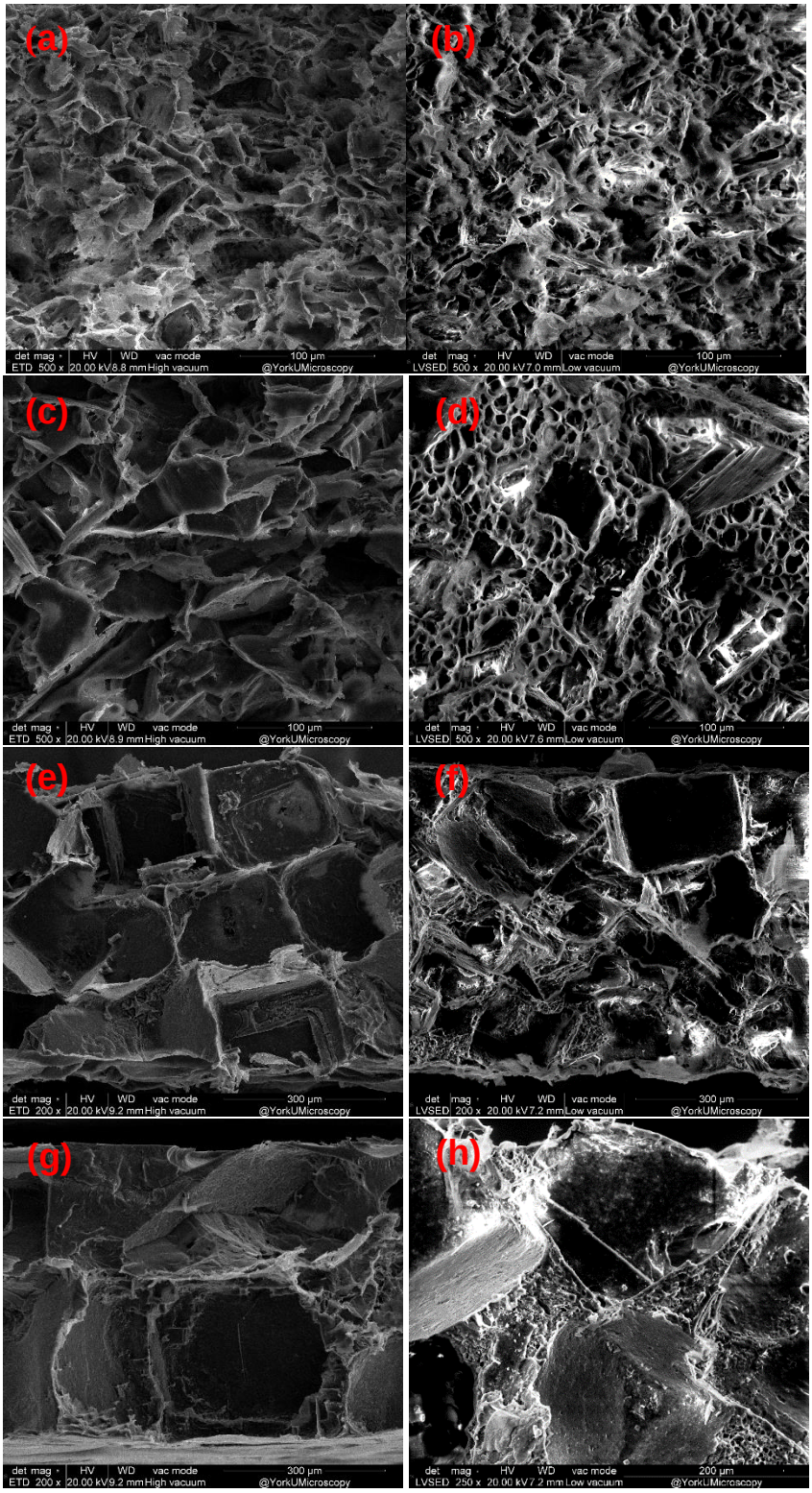


**Figure 4.14 Cross-section SEM images of open cell PVDF structures. Salt size less than 53 µm, (a) before and (b) after post-treatment, salt size 53-106 µm (c) before and (d) after post-treatment, salt size 106-250 µm (e) before (f) after post-treatment and salt size 250-500 µm (g) before and (h) after post-treatment.**

## 4.4 Conclusion

In summary, based on the combination of electro-poling, non-isothermal crystallization, and $ScCO_2$ processing, the electroactive phase content of PVDF greatly increased. PVDF foam structure with high electroactive phase content showed a better ability to generate TENG electrical outputs when compared to solid PVDF with lower electroactive phase content. Electroactive phase content of PVDF after $ScCO_2$ processing, non-isothermal crystallization and $ScCO_2$ processing, and combination of electro-poling and non-isothermal crystallization and $ScCO_2$ processing were 34.5%, 62.8% and 72%, respectively. TENG performance of different films revealed that electroactive phase content directly affected TENG output electrical signals. This is because of the increase in the difference between the Fermi levels of Al foil and PVDF as a result of a higher potential difference between the friction layers. On the other hand, foam structures led to an increase in ratio of surface area to volume and charge density of PVDF film. The final open circuit voltage and short circuit current increased from 16.9 V and 1.56 $mA/m^2$ for solid PVDF (electroactive content 36.6%) to 61 V and 5.27 $mA/m^2$ for PVDF after electro-poling and non-isothermal crystallization and $ScCO_2$ processing (electroactive content 72%). Moreover, non-isothermal crystallization and $ScCO_2$ processing were applied to open cell PVDF and led to an increase in electroactive content from ~42% to ~62% and introducing additional small pores with a size average of 20 $\mu$m to structure. TENG's performance of open cell PVDF improved in most cases as a result of both higher electroactive content and ratio of surface area to volume. This study unambiguously elucidates the feasibility of electro-poling and non-isothermal crystallization and $ScCO_2$ processing for fabrication of PVDF foam morphology with high electroactive content in order to improve TENG efficiency.

# Chapter 5 Electrospun PVDF Film

This chapter investigates the effects of electrospinning and chitin particles on the PVDF electroactive phase content and the PVDF film's triboelectric properties. Chitin is a structural polymer that is extracted from shellfish, insects or other microorganisms. Chitin is an abundant, biocompatible polymer with antibacterial properties [58-59]. Moreover, chitin is able to reinforce mechanical properties of PVDF fibers [60]. Electrospinning is a well-known fabrication method to prepare fibrous polymeric films. Electrospun films are quite thin, porous and their modification by altering various processing parameters is easy. In the end, the effect of chitin on PVDF electrospun films and triboelectric properties were studied.

## 5.1 Experimental

### 5.1.1 Materials

PVDF powder (Kynar 741, from Arkema) was used to prepare electrospinning solution. N, N-dimethyl formamide (DMF, Fisher Scientific) was used as polymer solvent and chitin was purchased from BOCO Technology Incorporation. Commercial aluminum foil was used as positive side of friction layer and at the same time as positive electrode. Copper tape with conductive adhesive on one side acted as negative side electrode and double side tape was used in order to mount electrodes on substrates.

### 5.1.2 Fabrication of electrospun films

A conventional horizontal electrospinning system was used to fabricate PVDF electrospun film. Polymer solution with a concentration of 20 wt.% was made by adding PVDF powder to 20 cc DMF. Polymer dissolved in DMF at room temperature using a magnetic stirrer spun at 200 rpm for two hours. The polymer solution was filled into a 10 ml syringe fitted with stainless steel

dispensing needles with various diameters of 0.58, 0.48 and 0.25 mm. A syringe pump (model LEGATO 100, KD Scientific) was used to feed the needle with flow rates of 1, 2 or 3 mL/hr. A high voltage power supply (Gamma High Voltage Research, Ormond Beach, FL) provided deriving force to stretch fibers by generating a constant voltage of 15 kV or 25 kV during electrospinning process. The positive electrode was connected to the needle while the negative electrode was connected to the aluminum foil collector (side lengths of 4 × 5 cm), which was placed 15 cm away from needle's tip. Electrospinning time span kept at 3 hours for all the samples. To investigate the effect of chitin on electrospun PVDF films, different amounts of chitin, ranging from 0 to 1.25 wt.%, were added to 20 cc DMF and the mixture was sonicated for two minutes. Subsequently, 4.7 g of PVDF was added to the solution. After proper mixing for 2 hours using a 200 rpm magnetic stirrer, the same electrospinning setup was used to prepare the samples.

**5.2 Characterization**

Crystallinity of PVDF samples was studied using a differential scanning calorimetry machine (DSC 250, TA Instrument). Thermal analyses were conducted from 40 ℃ to 220 ℃ at a ramping rate of 10 ℃/min. The degree of crystallinity ($X_c$) was calculated using equation 5.1:

$$X_c = \frac{\Delta H_f}{\Delta H_{f,c}} \times 100\% \qquad \text{(Eq. 5.1)}$$

where $\Delta H_f$ and $\Delta H_{f,c}$ are the heat of fusion of PVDF samples and heat of fusion of 100% crystalline PVDF which is 104.7 J/gr.

The rest of the characterization methods were done similar to chapter four and the same hammer setup as Figure 4.2 was used to drive TENG and investigate the effect of electrospinning on triboelectric properties of PVDF.

## 5.3 Results and Discussion

Various electrospinning parameters were chosen to study their effects on PVDF fibrous film, electroactive phase content and degree of crystallinity. In the end, the best films prepared with pure PVDF and PVDF-chitin were chosen to study how chitin can improve the triboelectric properties of PVDF films.

### 5.3.1 Effect of Feeding Rate on PVDF Electrospun Films

PVDF electrospun films were prepared using feeding rate of 1, 2 and 3 mL/hr. The voltage was kept constant at 15 kV and the needle with diameter of 0.58 mm was used. As shown in Figure 5.1(a), FTIR results showed that electrospun films prepared using a flow rate of 1 mL/hr possessed higher $\beta$ phase content. Indeed, a low feeding rate was favorable for the formation of $\beta$ polymorph since it led to higher stretching of fibers which helped to orient polymer chains toward $\beta$ structure [21].

A delicate stretch of fibers by electrospinning facilitate crystallization and as DSC results in Figure 5.1 (b) and SEM micrographs show lower feeding rate would result in a higher degree of crystallization [61].

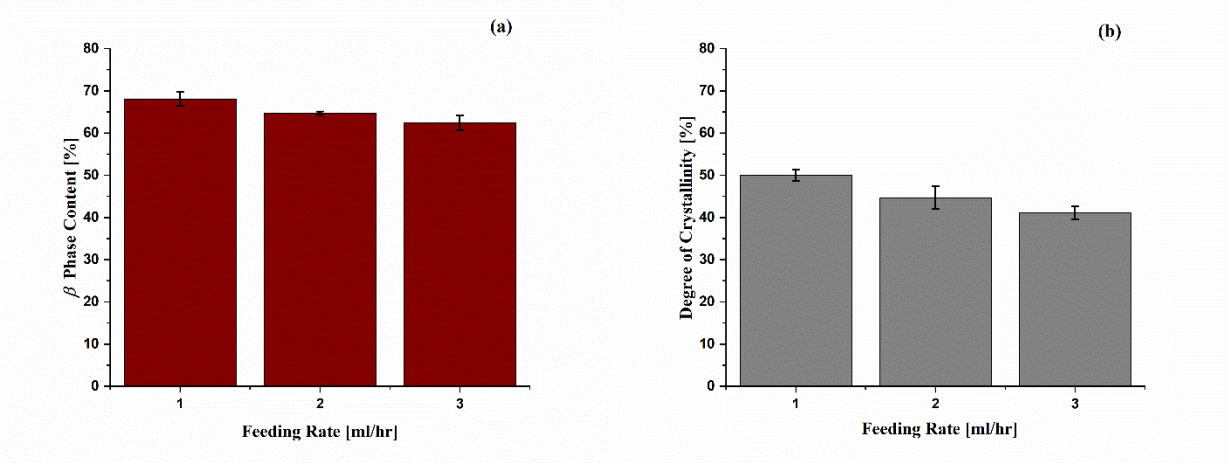


**Figure 5.1 Effect of electrospinning feeding rate on (a) electroactive content of PVDF and (b) degree of crystallinity.**

SEM images in Figure 5.2 reveal that an increase in the feeding rate significantly increased the number of beads in fibrous films. This could be attributed to lower capability of the electric field in higher feeding rates to finely stretch the fibers. As a result, higher feeding rate negatively affected the density of fibers.

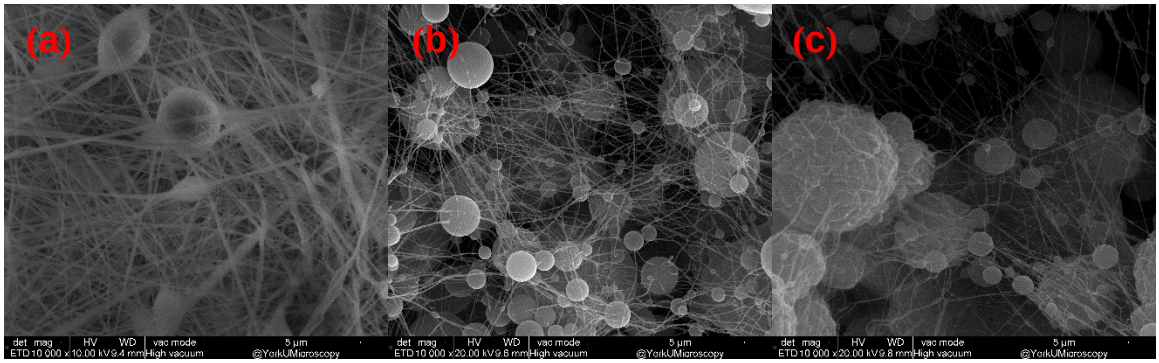


**Figure 5.2 SEM micrographs of electrospun films prepared by different feeding rate: (a) 1ml/hr, (b) 2 ml/hr and (c) 3 ml/hr.**

Moreover, influences of needle size on crystal structure and the average of electroactive phase content were investigated and the results showed that their effects were negligible.

### 5.3.2 Effect of Applied Voltage on PVDF Electrospun Films

In order to illustrate the effect of high voltage on the electroactive phase content and the degree of crystallinity of PVDF, electrospun films were prepared using voltage of 15 and 25 kV. Feeding rate, tip to collector distance and needle size were kept constant at 1 mL/hr, 15 cm and 0.58 mm, respectively.

FTIR and DSC results showed in Figure 5.3 revealed that an increase in voltage would result in a decrease in the total electroactive phase content and at same time it would slightly enhance the degree of crystallinity.

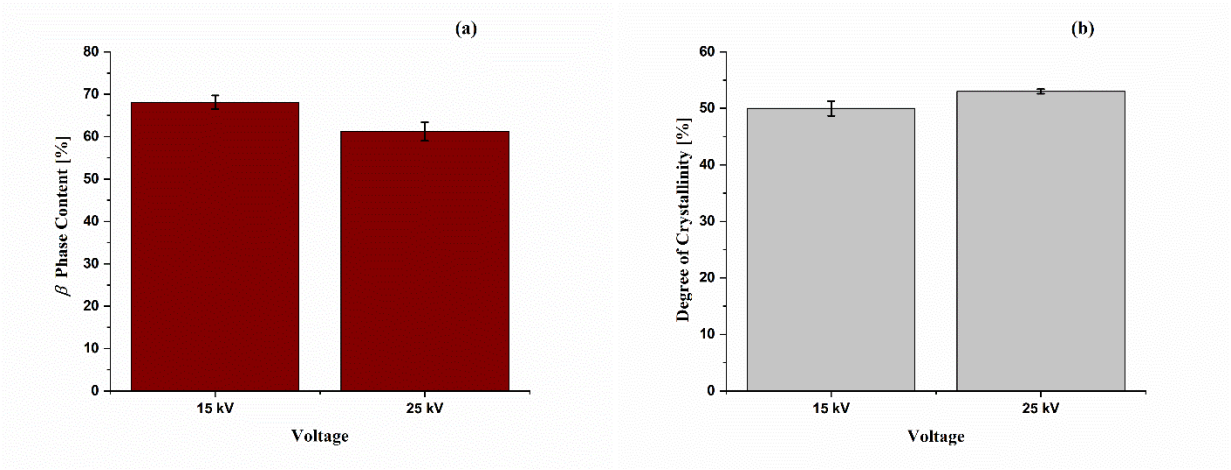


**Figure 5.3 Effect of high voltage on (a) electroactive content of PVDF and (b) degree of crystallinity.**

Although higher voltage would be favorable to control the orientation of polymer chains to form $\beta$ structure, the total electroactive phase content of samples decreased. This can be attributed to the instability of jet at higher voltages. Higher applied voltage leads to an increase in jet velocity and

removed droplets faster from the needle tip. Consequently, the volume of accumulated solution at the tip would decrease and Taylore cone shape at the tip will oscillate and became asymmetric. An increase in the degree of instability and oscillation of jet on needle's tip would result in lower electroactive phase content [49], [62].

### 5.3.3 Effect of Chitin Loads on PVDF Electrospun Films

Herein, different loads of chitin were added to 20wt.% PVDF solution to study its effect on the PVDF-based electrospun films.

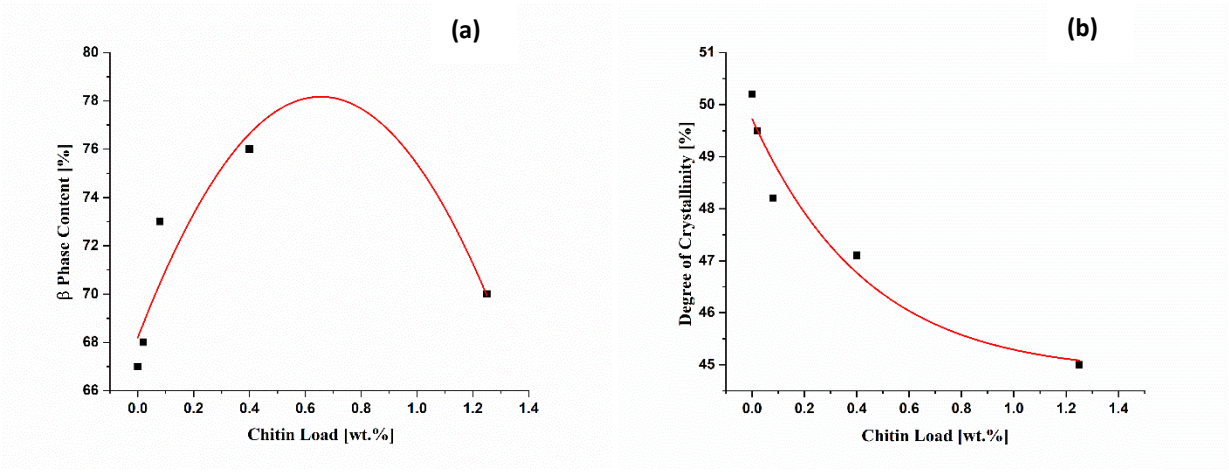


**Figure 5.4 Effect of chitin concentration on electroactive phase content of PVDF. (a) Electroactive content of PVDF and (b) degree of crystallinity.**

Figure 5.4 shows that chitin can improve the electroactive phase content of PVDF. Chitin is able to create hydrogen bonds with PVDF chains and through these hydrogen bonds it can rearrange the PVDF chain's to $\beta$ conformation, however, when chitin load passed 0.7 wt.%, $\beta$ phase content decreased drastically. This can be attributed to the aggregation of chitin particles in the electrospinning solution [63].

In contrast, an increase in chitin concentration would result in a decrease in the degree of crystallinity. This can be attributed to the limitation of PVDF chain movement in presence of chitin based on intermolecular interaction [60].

Furthermore, SEM micrographs in Figure 5.5 show that increasing the load of chitin led to an increase in the number of beads. This could be a side effect of chitin particle's aggregation.

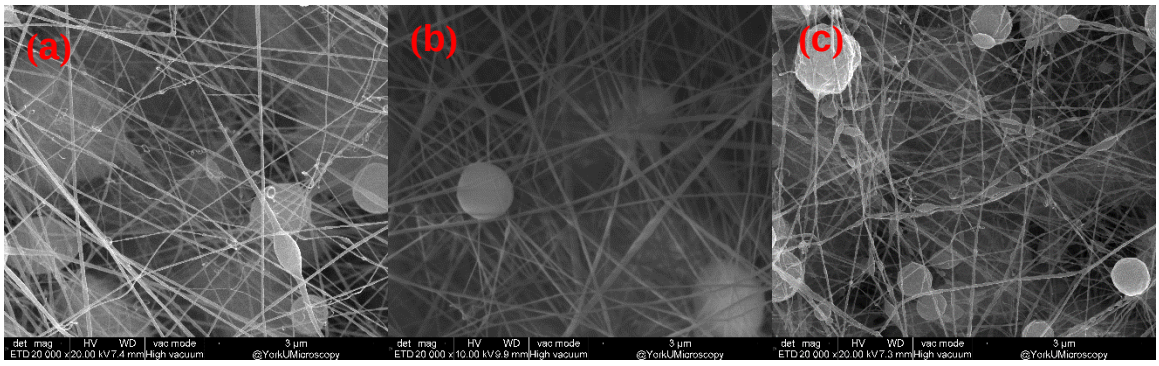


**Figure 5.5 Effect of chitin load on PVDF electrospun morphology. (a) 0.02 gr, (b) 0.1 gr and (c) 0.3 gr chitin in PVDF and DMF solution.**

### 5.3.4 Improvement of PVDF Triboelectric Properties Through Electrospinning

The effect of electrospinning and chitin on the triboelectric properties of PVDF were investigated. For this reason, PVDF films were prepared by electrospinning under 1 mL/h feeding rate, 15 kV of voltage, needle diameter of 0.58 mm, with and without 0.4 wt.% of chitin load.

Average of open circuit voltage and short circuit current density is shown in Figure 5.6 revealed that adding chitin into electrospun solution increased the electrical outputs of TENG around 5 V and 0.6 $mA/m^2$, respectively.

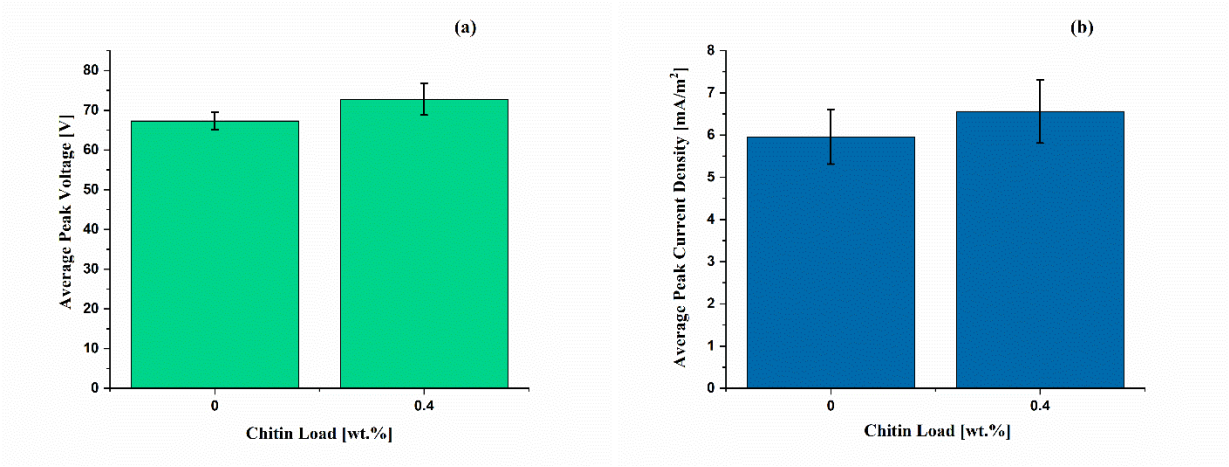


**Figure 5.6 Effect of electrospinning and chitin on electrical signal output of TENG: (a) average of voltage peaks and (b) average of current density peaks.**

It is worth mentioning here that the problem with pure PVDF electrospun films was their weak mechanical properties which made them tear during contact and separation, while chitin enhanced the strength of electrospun films significantly to the point where films would be able to withstand contact force for a longer period of time. Furthermore, PVDF-chitin electrospun films increased the average of $V_{oc}$ and $I_{sc}$ around 11.8 V and 1.2 mA/m$^2$, compared to the samples prepared through non-isothermal crystallization and $ScCO_2$ processing followed by electro-poling (chapter 4). Obviously, one can expect that the better performance of chitin-PVDF based electrospun films not only caused by their smaller thickness (thickness of around 30 μm) but also their higher electroactive phase contents. Moreover, these films were successfully used to directly light up at least 60 serially connected LEDs.

## 5.4 Conclusion

In this chapter, electrospinning was investigated as an easy and well-known processing method to improve the electroactive phase content of PVDF films and simultaneously electrical output of

TENG. Effect of some processing parameters such as feeding rate, needle size and voltage on PVDF electrospun films were studied in order to optimize the electrospinning process. Results showed that lower feeding rate and voltage were favorable to prepare finer fibers and enhanced electroactive phase content since fibers stretching would happen easier through lower feeding rate and also formed jet on needle tip in lower applied voltage was more stable. It was revealed that needle size would not tangibly affect the electroactive phase content and the degree of crystallinity of PVDF electrospun films.

In the second phase, chitin was added to the electrospinning solution and the results confirmed that chitin could improve the electroactive phase content of samples by creation of some hydrogen bonds with PVDF chains. Electroactive phase content of samples increased by 10% by the addition of 0.4 wt.% of chitin to 20 wt.% of PVDF solution. TENG results showed that chitin was able to increase the average open circuit voltage and short circuit current density around 5 V and 0.6 $mA/m^2$, respectively.

# Chapter 6 Contributions and Future Directions

## 6.1 Contributions

Triboelectric nanogenerators (TENGs) are newly found technology with vast potential applications to generate electricity by harvesting wasted mechanical energy. The aim of this research was to enhance TENG's output electrical signals through manipulation of friction layer.

PVDF was chosen as the negative side of friction layer since it has a high tendency to attract electrons while touches another dielectric material. Furthermore, the process of PVDF foam fabrication is industrially viable and on the other hand, PVDF tunable semi-crystal structure also makes it a unique candidate for TENG's friction layer.

Here we will first review the summary of results and discussion and show how TENG's performance improved step by step, then we will talk about the contribution and novelty of this research.

Here is a summary of results and discussions:

- Different geometry (*i.e.*, friction layer contact area and thickness) of PVDF solid films were used and the results showed that thinner friction layer with bigger size of contact area was able to generate higher electrical signals. Average of output voltage and current increased from 5.2 V and 0.29 μA for solid PVDF film (2 $cm^2$ of contact area and thickness of 0.5 mm) up to 30.1 V and 1.3 μA (for 8 $cm^2$ of contact area and thickness of 0.15 mm), respectively. This enhancement in TENG performance is mainly related to higher induction of electrostatic charges on electrodes through a thinner film and simultaneously higher capacity of thinner films with larger contact.

- Effect of PVDF open cell structure with different pore sizes in the range of <53, 53-106, 106-250 and 250-500 μm on TENG performance was studied. The results elucidated that the porous friction layer not only had significantly better performance rather than solid film but also smaller pore sizes were able to generate more electricity within contact and separation. Porous structure of PVDF has higher surface area to volume ratio and as the pores become smaller this ratio will increase further. Higher surface area to volume ratio provides more room for generation and storage of charge on the surface and promotes charge density and TENG electrical outputs. It is worth mentioning that the flexibility of PVDF porous structure provides friction layer the opportunity to compress more under the same mechanical force and as a result of thinner friction layer, enhanced TENG performance is expected.
- Effect of supercritical $CO_2$ processing (temperature profile one) on electroactive phase content of PVDF was studied. PVDF samples after temperature profile one possessed high volume expansion ratio, porous structure and around 34.5% of electroactive $\beta$ crystal phase.
- Effect of non-isothermal crystallization and supercritical $CO_2$ processing (temperature profile two) on electroactive phase content of PVDF was studied. High temperature and slower cooling rate in non-isothermal crystallization phase were favorable for the conformation of $\gamma$ crystal phase and after temperature profile two samples had smaller pores, lower VER and contained total electroactive phase content of around 62.8%.
- The presence of $\gamma$ crystal phase in temperature profile two led to a decrease in VER and pore size. This is mainly because of high compactness of $\gamma$ chains which encounters diffusion of $CO_2$ into structure and expansion of foam with difficulty.

- Electroactive phase of PVDF samples underwent temperature profile one and two promoted further through electro-poling under high voltage. Total electroactive phase content of PVDF increased around 10% after electro-poling as a result of rearrangement of polymer chains under electrical field.
- The effect of electroactive phase content of PVDF on TENG was investigated. Electrical output signals showed PVDF with high electroactive phase content possesses higher level of energy which leads to bigger energy difference between Fermi level of positive side of friction layer (*i.e.,* Al) and PVDF film. Consequently, there would be more room for transfer of triboelectric charges between two friction layers. Concisely, the final open circuit voltage and short circuit current density increased from 16.9 V and 1.56 $mA/m^2$ for solid PVDF (with electroactive phase content of 36.6%) to 61 V and 5.27 $mA/m^2$ for PVDF after electro-poling and temperature profile two (with electroactive phase content of 72%).
- The practicality of temperature profile two to promote electroactive phase content of open cell PVDF was studied and the results confirmed that treatment under temperature profile two can promote electroactive phase content of open cell PVDF around 13%.
- Finally, PVDF-chitin based electrospun friction layer was fabricated and through the hydrogen bond between chitin and PVDF chains electroactive phase content promoted to 78%. As a result of high electroactive phase content and thinner friction layer, the average of voltage and current density increased to 72.8 V and 6.47 $mA/m^2$, respectively.

Comparing TENG's performance from different works under different conditions is a challenge since so many parameters such as contact force, working mode, humidity of environment and *etc*. can directly affect the output results, however, here for a better overview Table 6.1 and 6.2

summarize how average of voltage and current density enhanced step by step through various techniques. The difference between two tables is only the TENG design that was used to collect electrical outputs. The design which was used to collect output signals for Table 6.1 was similar to Figure 3.2 with a smaller contact force, while TENG design that was used for data collection in Table 6.2 was schematically similar to Figure 4.2 with higher contact force.

**Table 6. 1 Summary of TENG's performance enhancement by changing the PVDF's geometrical and morphological parameters using TENG design similar to Figure 3.2.**

| **Fabrication method** | **Pore size (µm)** | **Contact area ($cm^2$)** | **Thickness (µm)** | **$\beta$ phase content (%)** | **$\gamma$ phase content (%)** | **Voltage (V)** | **Current Density ($mA/m^2$)** |
|---|---|---|---|---|---|---|---|
| Compression molding | Solid | 4 | 550 | 38.9 | 0 | 10.2 | 1.35 |
| Compression molding | Solid | 4 | 220 | 38.9 | 0 | 11.3 | 1.61 |
| Compression molding | Solid | 4 | 150 | 38.9 | 0 | 16.3 | 1.7 |
| Compression molding | Solid | 3.14 | 500 | 38.9 | 0 | 7.9 | 1.01 |
| Salt leaching | 250-500 | 3.14 | 500 | 41.6 | 0 | 7.4 | 1.03 |
| Salt leaching | 106-250 | 3.14 | 500 | 42.1 | 0 | 10 | 1.21 |
| Salt leaching | 53-106 | 3.14 | 500 | 41.3 | 0 | 14.4 | 1.71 |
| Salt leaching | <53 | 3.14 | 500 | 43.4 | 0 | 20.5 | 2.9 |
| Temperature profile one | 50 (closed cell) | 3.14 | 500 | 34.5 | 0 | 20.8 | 2.7 |

**Table 6. 2 Summary of TENG's performance enhancement by changing the PVDF's geometrical, morphological and electroactive phase content parameters using TENG design similar to Figure 4.2.**

| Fabrication method | Pore size (μm) | Contact area ($cm^2$) | Thickness (μm) | $\beta$ phase content (%) | $\gamma$ phase content (%) | Voltage (V) | Current Density ($mA/m^2$) |
|---|---|---|---|---|---|---|---|
| Compression molding | Solid | 3.14 | 500 | 36.6 | 0 | 16.9 | 1.56 |
| Temperature profile two without $ScCO_2$ processing | Solid | 3.14 | 500 | 9.2 | 51.1 | 27.5 | 1.97 |
| Temperature profile one | 11.7 | 3.14 | 500 | 34.5 | 0 | 46.4 | 3.77 |
| Temperature profile two | 4.36 | 3.14 | 500 | 51.2 | 11.6 | 53.9 | 5.1 |
| Temperature profile one and electro-poling | 5.3 | 3.14 | 150 | 53.9 | 0 | 59.5 | 4.2 |
| Temperature profile two and electro-poling | 2.3 | 3.14 | 220 | 61.6 | 10.4 | 61 | 5.3 |
| PVDF electrospun film | NA | 3.14 | 30 | 67 | 0 | 67.3 | 5.96 |
| PVDF-chitin electrospun film | NA | 3.14 | 30 | 76 | 0 | 72.8 | 6.56 |

Most of the researches focus only on one or two parameters in order to increase TENG's efficiency, while in this research TENG's performance improved step by step through a comprehensive study on TENG's effective parameters. This study was necessary in order to find the existing gaps for

future direction. For the first time, this study showed that TENG's electrical outputs are not related to the cell structure. In other words, regardless of using open cell or closed cell structure of PVDF film, TENG's electrical output is same as long as the average of cell sizes are almost equal. Also, most of the researches around electroactive phase content of PVDF are around promoting the $\beta$ phase crystal, however, this research confirmed that increasing in $\gamma$ phase crystal content can improve TENG's performance as well. Finally, fabrication of electrospun chitin-PVDF composite for TENG's friction layer was the other novelty of this research in order to enhance the output signals.

## 6.2 Future Direction

This research aimed to study effect of different parameters such as contact area, thickness, porosity, electroactive phase content and electrospinning on PVDF's triboelectric properties.

Here are some recommendations for the future direction of this research:

- The effect of geometry confirmed that an increase in solid PVDF contact area would result in an increase in open circuit voltages. Surprisingly, there is no evidence in references about the fundamentals behind the relation of contact area and TENG's output voltage. Most papers assume as the contact area increases the capacitance of friction layer and charge density will increase but the exact relationship between the capacitance of friction layer and surface charge density is needed to be elucidated in future.
- Fabrication of thinner porous structure with higher surface area to volume ratio by spin coating can be another solution to enhance TENG's output signals.
- Decreasing the electrospinning time in order to decrease the thickness of electrospun film can lead to higher degree of electrostatic induction and better TENG's performance.

- Using corona poling instead of electro-poling practically provides the opportunity to apply higher voltage on PVDF film without breaking it down and as a result, promotes the electroactive content of PVDF.
- Making a composite of PVDF with high dielectric nanoparticles (such as $TiO_2$, $BaTiO_3$ or $SrTiO_3$) can increase the total dielectric constant and triboelectric properties of PVDF.
- Most important potential direction for this research would be a creative design of TENG using PVDF films for harvesting wasted mechanical energy to power up a small electrical device or fabrication of self-powered sensor.

# References:


[1] Y. Hao, Y. Bin, H. Tao, W. Cheng, W. Hongzhi, and Z. Meifang, "Fluoride ( PVDF ) Triboelectric Nanogenerator via Electrospinning," vol. 1, pp. 1485–1488, 2015.

[2] N. Cui *et al.*, "Dynamic Behavior of the Triboelectric Charges and Structural Optimization of the Friction Layer for a Triboelectric Nanogenerator," *ACS Nano*, vol. 10, no. 6, pp. 6131–6138, 2016.

[3] Z. L. Wang, L. Lin, J. Chen, S. Niu, and Y. Zi, *Triboelectric Nanogenerators*. 2016.

[4] F. R. Fan, Z. Q. Tian, and Z. Lin Wang, "Flexible triboelectric generator," *Nano Energy*, vol. 1, no. 2, pp. 328–334, 2012.

[5] Z. L. Wang, "Triboelectric Nanogenerators as New Energy Technology for Self-Powered Systems and as Active Mechanical and Chemical Sensors," *ACS Nano*, vol. 7, no. 11, pp. 9533–9557, Nov. 2013.

[6] E. Fukada, "History and Recent Progress in," *Ieee Transduct. Ultrason. Freq. Control*, vol. 47, no. 6, pp. 1277–1289, 2000.

[7] J. E. Lee and S. N. Leung, "Multi-stage crystallization mechanism of electroactive phase polyvinylidene fluoride induced by thermal and supercritical carbon dioxide processing," vol. 20, no. 29, 2018.

[8] A. Salimi and A. A. Yousefi, "Analysis Method," *Polym. Test.*, vol. 22, no. 6, pp. 699–704, 2003.

[9] P. Martins, A. C. Lopes, and S. Lanceros-Mendez, "Electroactive phases of poly(vinylidene fluoride): Determination, processing and applications," *Prog. Polym. Sci.*, vol. 39, no. 4, pp. 683–706, 2014.

[10] J. W. Lee *et al.*, "Robust nanogenerators based on graft copolymers via control of dielectrics for remarkable output power enhancement," *Sci. Adv.*, vol. 3, no. 5, pp. 1–10, 2017.

[11] T. Li *et al.*, "Lightweight Triboelectric Nanogenerator for Energy Harvesting and Sensing Tiny Mechanical Motion," *Adv. Funct. Mater.*, vol. 26, no. 24, pp. 4370–4376, 2016.

[12] J. H. Lee, I. Yu, S. Hyun, J. K. Kim, and U. Jeong, "Remarkable increase in triboelectrification by enhancing the conformable contact and adhesion energy with a film-covered pillar structure," *Nano Energy*, vol. 34, no. December 2016, pp. 233–241, 2017.

[13] K. Y. Lee *et al.*, "Hydrophobic sponge structure-based triboelectric nanogenerator," *Adv. Mater.*, vol. 26, no. 29, pp. 5037–5042, 2014.

[14] G. Zhu *et al.*, "Triboelectric-generator-driven pulse electrodeposition for micropatterning," *Nano Lett.*, vol. 12, no. 9, pp. 4960–4965, 2012.

[15] F. R. Fan, L. Lin, G. Zhu, W. Wu, R. Zhang, and Z. L. Wang, "Transparent triboelectric nanogenerators and self-powered pressure sensors based on micropatterned plastic films," *Nano Lett.*, vol. 12, no. 6, pp. 3109–3114, 2012.

[16] X. He, H. Guo, X. Yue, J. Gao, Y. Xi, and C. Hu, "Improving energy conversion efficiency for triboelectric nanogenerator with capacitor structure by maximizing surface charge density," *Nanoscale*, vol. 7, no. 5, pp. 1896–1903, 2015.

[17] V. Sencadas, M. V. Moreira, S. Lanceros-Méndez, A. S. Pouzada, and R. Gregório Filho, "α- to β Transformation on PVDF Films Obtained by Uniaxial Stretch," *Mater. Sci. Forum*, vol. 514–516, pp. 872–876, May 2006.

[18] T. Hattori, M. Kanaoka, and H. Ohigashi, "Improved piezoelectricity in thick lamellar β-form crystals of poly(vinylidene fluoride) crystallized under high pressure," *J. Appl. Phys.*, vol. 79, no. 4, pp. 2016–2022, Feb. 1996.

[19] H.-J. Ye, W.-Z. Shao, and L. Zhen, “Crystallization kinetics and phase transformation of poly(vinylidene fluoride) films incorporated with functionalized baTiO 3 nanoparticles,” *J. Appl. Polym. Sci.*, vol. 129, no. 5, pp. 2940–2949, Sep. 2013.
[20] A. Gradys, P. Sajkiewicz, S. Adamovsky, A. Minakov, and C. Schick, “Crystallization of poly(vinylidene fluoride) during ultra-fast cooling,” *Thermochim. Acta*, vol. 461, no. 1–2, pp. 153–157, Sep. 2007.
[21] J. Zheng, A. He, J. Li, and C. C. Han, “Polymorphism Control of Poly(vinylidene fluoride) through Electrospinning,” *Macromol. Rapid Commun.*, vol. 28, no. 22, pp. 2159–2162, Nov. 2007.
[22] Y. Wang, X. Zhou, Q. Chen, B. Chu, and Q. Zhang, “Recent development of high energy density polymers for dielectric capacitors,” *IEEE Trans. Dielectr. Electr. Insul.*, vol. 17, no. 4, pp. 1036–1042, Aug. 2010.
[23] S. Wang, L. Lin, and Z. L. Wang, “Nanoscale triboelectric-effect-enabled energy conversion for sustainably powering portable electronics,” *Nano Lett.*, vol. 12, no. 12, pp. 6339–6346, 2012.
[24] S. Wang, L. Lin, Y. Xie, Q. Jing, S. Niu, and Z. L. Wang, “Sliding-triboelectric nanogenerators based on in-plane charge-separation mechanism,” *Nano Lett.*, vol. 13, no. 5, pp. 2226–2233, 2013.
[25] G. Zhu *et al.*, “Linear-grating triboelectric generator based on sliding electrification,” *Nano Lett.*, vol. 13, no. 5, pp. 2282–2289, 2013.
[26] Y. Yang, Y. S. Zhou, H. Zhang, Y. Liu, S. Lee, and Z. L. Wang, “A single-electrode based triboelectric nanogenerator as self-powered tracking system,” *Adv. Mater.*, vol. 25, no. 45, pp. 6594–6601, 2013.
[27] Y. Yang *et al.*, “Single-electrode-based sliding triboelectric nanogenerator for self-powered displacement vector sensor system,” *ACS Nano*, vol. 7, no. 8, pp. 7342–7351, 2013.
[28] S. Niu *et al.*, “Theoretical investigation and structural optimization of single-electrode triboelectric nanogenerators,” *Adv. Funct. Mater.*, vol. 24, no. 22, pp. 3332–3340, 2014.
[29] S. Wang, Y. Xie, S. Niu, L. Lin, and Z. L. Wang, “Freestanding triboelectric-layer-based nanogenerators for harvesting energy from a moving object or human motion in contact and non-contact modes,” *Adv. Mater.*, vol. 26, no. 18, pp. 2818–2824, 2014.
[30] S. Wang, S. Niu, J. Yang, L. Lin, and Z. L. Wang, “Quantitative measurements of vibration amplitude using a contact-mode freestanding triboelectric nanogenerator,” *ACS Nano*, vol. 8, no. 12, pp. 12004–12013, 2014.
[31] S. Niu *et al.*, “Theoretical study of contact-mode triboelectric nanogenerators as an effective power source,” *Energy Environ. Sci.*, vol. 6, no. 12, p. 3576, 2013.
[32] J. M. Wu, C. K. Chang, and Y. T. Chang, “High-output current density of the triboelectric nanogenerator made from recycling rice husks,” *Nano Energy*, vol. 19, pp. 39–47, 2016.
[33] *Processing and Finishing of Polymeric Materials*. Wiley, 2012.
[34] X. F. Huisheng Peng, Xuemei Sun, Wei Weng, “Polymer Materials for Energy and Electronic Applications,” Academic Press, 2016.
[35] M. Wang *et al.*, “Single-electrode triboelectric nanogenerators based on sponge-like porous PTFE thin films for mechanical energy harvesting and self-powered electronics,” *J. Mater. Chem. A*, vol. 5, no. 24, pp. 12252–12257, 2017.
[36] P. Bai *et al.*, “Dipole-moment-induced effect on contact electrification for triboelectric nanogenerators,” vol. 7, no. 7, pp. 990–997, 2014.
[37] J. Chen *et al.*, “Enhancing Performance of Triboelectric Nanogenerator by Filling High

Dielectric Nanoparticles into Sponge PDMS Film," *ACS Appl. Mater. Interfaces*, vol. 8, no. 1, pp. 736–744, 2016.
[38] S. H. Shin, Y. H. Kwon, Y. H. Kim, J. Y. Jung, M. H. Lee, and J. Nah, "Triboelectric charging sequence induced by surface functionalization as a method to fabricate high performance triboelectric generators," *ACS Nano*, vol. 9, no. 4, pp. 4621–4627, 2015.
[39] S. Wang *et al.*, "Maximum surface charge density for triboelectric nanogenerators achieved by ionized-air injection: Methodology and theoretical understanding," *Adv. Mater.*, vol. 26, no. 39, pp. 6720–6728, 2014.
[40] K. Y. Lee *et al.*, "Controllable Charge Transfer by Ferroelectric Polarization Mediated Triboelectricity," pp. 3067–3073, 2016.
[41] N. Soin *et al.*, "High performance triboelectric nanogenerators based on phase-inversion piezoelectric membranes of poly(vinylidene fluoride)-zinc stannate (PVDF-ZnSnO3) and polyamide-6 (PA6)," *Nano Energy*, vol. 30, no. August, pp. 470–480, 2016.
[42] R. Simpkin, "Derivation of Lichtenecker ' s Logarithmic Mixture Formula From Maxwell ' s Equations," vol. 58, no. 3, pp. 545–550, 2010.
[43] L. Li, M. Zhang, M. Rong, and W. Ruan, "Studies on the transformation process of PVDF from α to β phase by stretching," *RSC Adv.*, vol. 4, no. 8, pp. 3938–3943, 2014.
[44] S. Satapathy, S. Pawar, P. K. Gupta, and K. B. RVarma, "Effect of annealing on phase transition in poly(vinylidene fluoride) films prepared using polar solvent," *Bull. Mater. Sci.*, vol. 34, no. 4, pp. 727–733, 2011.
[45] W. M. Prest and D. J. Luca, "The formation of the γ phase from the α and β polymorphs of polyvinylidene fluoride," *J. Appl. Phys.*, vol. 49, no. 10, pp. 5042–5047, Oct. 1978.
[46] R. Gregorio, "Determination of the α, β, and γ crystalline phases of poly(vinylidene fluoride) films prepared at different conditions," *J. Appl. Polym. Sci.*, vol. 100, no. 4, pp. 3272–3279, May 2006.
[47] Y. Oka and N. Koizumi, "Formation of Unoriented Form I Poly (vinylidene fluoride) by High-Rate Quenching and its Electrical Properties," *Bull. Inst. Chem. Res., Kyoto Univ*, vol. 63, no. 3, 1985.
[48] J. Scheinbeim, C. Nakafuku, B. A. Newman, and K. D. Pae, "High-pressure crystallization of poly(vinylidene fluoride)," *J. Appl. Phys.*, vol. 50, no. 6, pp. 4399–4405, Jun. 1979.
[49] C. Ribeiro, V. Sencadas, J. L. G. Ribelles, and S. Lanceros-Méndez, "Influence of Processing Conditions on Polymorphism and Nanofiber Morphology of Electroactive Poly(vinylidene fluoride) Electrospun Membranes," *Soft Mater.*, vol. 8, no. 3, pp. 274–287, Sep. 2010.
[50] P. Thakur, A. Kool, B. Bagchi, N. A. Hoque, S. Das, and P. Nandy, "In situ synthesis of Ni(OH) 2 nanobelt modified electroactive poly(vinylidene fluoride) thin films: remarkable improvement in dielectric properties," *Phys. Chem. Chem. Phys.*, vol. 17, no. 19, pp. 13082–13091, 2015.
[51] T. Miyazaki, Y. Takeda, M. Akasaka, M. Sakai, and A. Hoshiko, "Preparation of Isothermally Crystallized γ-Form Poly(vinylidene fluoride) Films by Adding a KBr Powder as a Nucleating Agent," *Macromolecules*, vol. 41, no. 7, pp. 2749–2753, Apr. 2008.
[52] Jean Cross, *Electrostatics : principles, problems and applications*. Bristol: IOP Publishing : Hilger, 1987.
[53] R. C. C. R. Gregorio, "Morphology and phase transition of high melt temperature crystallized poly ( vinylidene fluoride )," *J. Mater. Sci.*, vol. 35, no. 2, pp. 299–306, 2000.
[54] J. Liu, X. Lu, and C. Wu, "Effect of Preparation Methods on Crystallization Behavior and

Tensile Strength of Poly(vinylidene fluoride) Membranes," *Membranes (Basel).*, vol. 3, no. 4, pp. 389–405, Nov. 2013.
[55] X. Cai, T. Lei, D. Sun, and L. Lin, "A critical analysis of the α, β and γ phases in poly(vinylidene fluoride) using FTIR," *RSC Adv.*, vol. 7, no. 25, pp. 15382–15389, 2017.
[56] V. Nguyen and R. Yang, "Effect of humidity and pressure on the triboelectric nanogenerator," *Nano Energy*, vol. 2, no. 5, pp. 604–608, 2013.
[57] J. E. Lee, Y. Guo, R. E. Lee, and S. N. Leung, "Fabrication of electroactive poly(vinylidene fluoride) through non-isothermal crystallization and supercritical $CO_2$ processing," *RSC Adv.*, vol. 7, no. 77, pp. 48712–48722, 2017.
[58] M. Paillet and A. Dufresne, "Chitin Whisker Reinforced Thermoplastic Nanocomposites," *Macromolecules*, vol. 34, no. 19, pp. 6527–6530, Sep. 2001.
[59] A. Qin, X. Li, X. Zhao, D. Liu, and C. He, "Preparation and characterization of nano-chitin whisker reinforced PVDF membrane with excellent antifouling property," *J. Memb. Sci.*, vol. 480, pp. 1–10, Apr. 2015.
[60] J. Junkasem, R. Rujiravanit, B. P. Grady, and P. Supaphol, "X-ray diffraction and dynamic mechanical analyses of Î±-chitin whisker-reinforced poly(vinyl alcohol) nanocomposite nanofibers," *Polym. Int.*, vol. 59, no. 1, pp. 85–91, Jan. 2010.
[61] L. M. M. Costa, R. E. S. Bretas, and R. Gregorio, "Effect of Solution Concentration on the Electrospray/Electrospinning Transition and on the Crystalline Phase of PVDF," *Mater. Sci. Appl.*, vol. 01, no. 04, pp. 247–252, 2010.
[62] X. Zong, K. Kim, D. Fang, S. Ran, B. S. Hsiao, and B. Chu, "Structure and process relationship of electrospun bioabsorbable nanofiber membranes," *Polymer (Guildf).*, vol. 43, no. 16, pp. 4403–4412, Jul. 2002.
[63] N. A. Hoque *et al.*, "Biowaste crab shell-extracted chitin nanofiber-based superior piezoelectric nanogenerator," *J. Mater. Chem. A*, vol. 6, no. 28, pp. 13848–13858, 2018.